

Superhard oxidation-resistant $\text{Ti}_{1-x}\text{Al}_x\text{B}_y$ thin films grown by hybrid HiPIMS/DCMS co-sputtering diboride targets without external substrate heating

B. Wicher^{a,b,*}, O.V. Pshyk^{a,c}, X. Li^a, B. Bakhit^a, V. Rogoz^{a,d}, I. Petrov^{a,e}, L. Hultman^{a,d}, G. Greczynski^{a,d}

^a Thin Film Physics Division, Department of Physics (IFM), Linköping University, Linköping SE-58183, Sweden

^b Faculty of Materials Science and Engineering, Warsaw University of Technology, 141 Woloska St., 02-507 Warsaw, Poland

^c Laboratory for Surface Science and Coating Technology, Empa, Swiss Federal Laboratories for Materials Science and Technology, Ueberlandstrasse 129, 8600 Dübendorf, Switzerland

^d Wallenberg Initiative Materials Science for Sustainability, WISE, Linköping University

^e Materials Research Laboratory, University of Illinois, Urbana, IL 61801, United States

ARTICLE INFO

Keywords:

Transition metal diboride thin films
Mechanical properties
Oxidation resistance
Magnetron sputtering
HiPIMS
Ion mass spectrometry

ABSTRACT

$\text{Ti}_{1-x}\text{Al}_x\text{B}_y$ films ($0.40 \leq x \leq 0.76$, and $1.81 \leq y \leq 2.03$) combining good mechanical properties and high-temperature oxidation resistance are demonstrated. Layers are grown using a hybrid high-power impulse and dc magnetron co-sputtering employing two target configurations (AlB_2 -HiPIMS/ TiB_2 -DCMS and TiB_2 -HiPIMS/ AlB_2 -DCMS) and no external substrate heating. Near-stoichiometric B content are achieved by co-sputtering two diboride targets. Time-resolved ion mass spectrometry analyses reveal that the ionization of the DCMS flux (Al) is much higher during TiB_2 -HiPIMS/ AlB_2 -DCMS. The effect is caused by the difference in the first ionization potentials and the ionization probabilities of sputtered metals and results in lower B/metal ratios in films grown in this configuration. The B/metal ratio in the single-phase $\text{Ti}_{1-x}\text{Al}_x\text{B}_y$ decreases with increasing Al content, which is explained by the change between angular distribution of Ti and Al atoms. Alloying with Al improves the high-temperature oxidation resistance: the thickness of the oxide-scale forming after 1 h anneal at 800 °C decreases more than 15 times upon increasing x from 0.36 to 0.74. $\text{Ti}_{1-x}\text{Al}_x\text{B}_y$ films with $0.58 \leq x \leq 0.67$ offer the best compromise between high-temperature oxidation resistance and mechanical properties with an average oxide scale thickness 90–180 nm and the hardness of 34–38 GPa.

1. Introduction

Transition-metal diborides (TMB_2) typically crystallize in a hexagonal AlB_2 -type structure (P6/mmm, SG-191) [1], in which the B atoms form sheets between hexagonal-close-packed TM layers. TMB_2 exhibit a unique combination of functional properties such as high melting points [2], high hardness [3], good wear resistance, and high chemical and thermal stability [4]. These features, which mainly originate from the dual ceramic/metallic chemical-bonding nature of TMB_2 - strong covalent bonding between TM and B atoms and within the B sheets as well as metallic bonding within TM layers, make TMB_2 desirable candidates for cutting tool applications [5,6]. However, compared to widely used TM-based nitrides [7], the industrial applications of sputter-deposited TM

diborides are still lagging, primarily due to difficulties with stoichiometry control, limited fracture toughness [8,9], and poor oxidation resistance [10].

Synthesis of TiB_y thin films is commonly carried out using stoichiometric TiB_2 targets in a direct-current magnetron sputtering (DCMS) system. Mayrhofer et al. [11] showed that such films are over-stoichiometric with B/metal ratio, y, $2.1 \leq y \leq 3.2$, composed of 001-oriented nanocolumns encapsulated in the amorphous B-rich tissue phase [12]. Segregation of surplus B to grain boundaries observed within $\text{TiB}_{y>2.1}$ layers provides outstanding hardness (H), often above 40 GPa [13].

Another approach that allows to control of the TiB_y stoichiometry is based on high-power impulse magnetron sputtering (HiPIMS) [14].

* Corresponding author.

E-mail address: bartosz.wicher@liu.se (B. Wicher).

<https://doi.org/10.1016/j.matdes.2024.112727>

Received 21 November 2023; Received in revised form 5 January 2024; Accepted 1 February 2024

Available online 5 February 2024

0264-1275/© 2024 The Author(s). Published by Elsevier Ltd. This is an open access article under the CC BY license (<http://creativecommons.org/licenses/by/4.0/>).

During HiPIMS the power to the magnetron is applied in short (20–100 μ s) pulses with high amplitude while maintaining the average power on the similar level as during conventional DCMS [15–19]. This creates high density plasma in front of the magnetron thus increasing probability for electron impact ionization of the sputter-ejected target atoms [20]. In consequence, a significant portion of the sputtered flux becomes ionized [21] allowing for precise control of energy and momentum of film constituents through the application of a substrate bias. With this method, the B/Ti ratio can be varied from 2.08 to 1.83 by varying the HiPIMS pulse length at a substrate temperature, T_s , of 450 °C (while maintaining all other parameters constant), which results in a large variation of the peak target current density and, hence, the extent of gas rarefaction effects [22]. The latter increase with decreasing the pulse length (increasing the peak target current) such that the film growth becomes controlled by an ionized fraction of the sputtered material flux (rather than neutrals as in DCMS) steered then to the substrate to preserve plasma neutrality. Under such conditions, the Ti metal fraction in the film increases as Ti is overrepresented in the ionized flux due to a lower ionization potential than that of B [23]. Understoichiometric $\text{TiB}_{1.43}$ film obtained with this method under the heated substrate conditions at 670 °C consists of columnar grains lacking B segregation at column boundaries, with the B-deficiency present as Ti-rich planar defects [24], and reveals a nanoindentation superhardness, $H = 43.9 \pm 0.9$ GPa [25].

Several deposition approaches launched at the elevated temperatures, including unique co-sputtering target configurations [26,27], have been widely used to control the composition and microstructure of alloyed TMB_2 films. Monclus et al. [28] co-sputtered nanocrystalline $\text{Ti}_{1-x}\text{Al}_x\text{B}_y$ films with B/Al ratio = 14.9 from TiAl and TiB_2 targets at a T_s reaching max. ~ 170 °C and showed that even small incorporation of Al into the nanocrystalline TiB_2 layers increased the H to elastic modulus, E , ratio (H/E), for metal-rich $\text{Ti}_{1-x}\text{Al}_x\text{B}_y$ with $y < 1.60$ [29]. Thornberg et al. [30] sputtered a segmented TiB_2 - AlB_2 target in Ar and Kr gas mixtures at T_s varying from 230 to 440 °C, and found a decrease in H and E with increasing the Al/(Ti + Al) content, x , from 0.1 to 0.7, for the B-deficient $\text{Ti}_{1-x}\text{Al}_x\text{B}_{1.3}$. The $\text{Ti}_{0.9}\text{Al}_{0.1}\text{B}_y$ thin films also showed better nanoindentation toughness when the B content decreased from $y = 1.9$ to 1.3. Co-sputtering TiB_2 and Al targets kept at a $T_s = 180$ °C allowed Stüber et al. [31] to synthesize a single-phase $\text{Ti}_{1-x}\text{Al}_x\text{B}_y$ solid solutions with $y \sim 2$ and $0.1 < x < 0.16$ on the cemented carbide substrates, with H values above 30.8 GPa. A formation of the Al-enriched B-tissue phase at a $T_s = 240$ °C was, in turn, presented in a series of $\text{Ti}_{1-x}\text{Al}_x\text{B}_y$ layers with a further increased Al fraction, $0.20 \leq x \leq 0.45$, by Nedfors et al. [32]. The formation of tissue phase with quenched grain growth in the in-plane direction results then in the highest H of 39 GPa, demonstrated for the case of $\text{Ti}_{0.79}\text{Al}_{0.21}\text{B}_{2.70}$ solid solution. $\text{Ti}_{1-x}\text{Al}_x\text{B}_y$ films with even higher Al content, $x = 0.3$ – 0.66 and $y = 2.07$ – 3.22 were grown at a $T_s = 400$ °C from TiB_2 and AlB_2 targets in the study of Mockute et al. [33]. In the latter study, an increase in x resulted in a significant drop in H , from 28 GPa with $\text{Ti}_{0.70}\text{Al}_{0.30}\text{B}_{3.22}$ to only 14 GPa with $\text{Ti}_{0.34}\text{Al}_{0.66}\text{B}_{2.07}$ due to a surface-initiated isostructural phase decomposition into Ti- and Al-rich diboride domains.

The applications of sputter-deposited TiB_2 films are, however, limited due to a poor high-temperature oxidation resistance leading easily to failure already at 400 °C [34]. The oxidation kinetics of DCMS-deposited $\text{TiB}_{2.4}$ showed a linear type behavior, resulting from the $\text{B}_2\text{O}_3(\text{g})$ oxide phase formation, causing diboride films to be oxidized with the formation of an ~ 1900 -nm oxide scale [35]. To improve the poor oxidation resistance TMB_2 alloying with Al [36] or Si [37] was offered to form a protective alumina- or silica-containing scales which passivated the surface. As a result, a parabolic oxidation type with a significantly decreased O diffusion rate at 700 °C up to 8 h was presented for co-sputtered Al-HiPIMS/ TiB_2 -DCMS $\text{Ti}_{0.68}\text{Al}_{0.32}\text{B}_{1.35}$ film alloy at a $T_s \sim 475$ °C [35]. However, the inclusion of Al in the as-deposited state resulted in H decrease, from 43 GPa in the $\text{TiB}_{2.4}$ to 37 GPa for the $\text{Ti}_{0.68}\text{Al}_{0.32}\text{B}_{1.35}$. Similarly, Si additions at a T_s of 550 °C result in the

formation of a dense SiO_2 scale at the expense of mechanical properties for $\text{TM}(\text{Cr}, \text{Ti}, \text{W}, \text{Hf})\text{-Si}_{0.15}\text{-B}_{1.88 \leq y \leq 2.72}$ [38].

Thus, alloying TiB_x thin films with Al is a promising route toward improved oxidation resistance. The accompanying deterioration of mechanical properties stems from poor control over the B stoichiometry (severe B deficiency) and film nanostructure, primarily when the TiB_2 and metal (Al or TiAl) targets are used for sputter-codeposition.

To resolve the issue of severe B-deficiency, while employing Al alloying for better high temperature oxidation resistance, we apply the hybrid HiPIMS/DCMS co-sputtering from diboride targets employing metal-ion-synchronized biasing with the HiPIMS pulse, which provides much-improved control (compared to DCMS) over the energy and the momentum of ionized species incident at the growing film surface. This technique relies on the inherent time separation of gas and metal ion fluxes at the substrate plane, which is an early recognized characteristic feature of HiPIMS [39]. Ion energy and momentum are controlled by the amplitude of the bias pulse, which is applied during the time the metal-to-gas ion ratio is at maximum value. At all other times substrates are electrically floating to minimize entrapment of gas ions and, hence, reduce the residual compressive stress levels [40,41]. Here, two sets of experiments are carried out. In the first case, the AlB_2 target is powered with HiPIMS, while the TiB_2 target works in DCMS mode. The positions of targets are then switched for the second set of experiments. $\text{Ti}_{1-x}\text{Al}_x\text{B}_y$ alloys with $0.40 \leq x \leq 0.76$ and $1.81 \leq y \leq 2.03$ are, thus, grown with the assistance of Ti^+ and Al^+ metal ion irradiation. In order to minimize the energy consumption, all films are grown with no external substrate heating.

2. Experimental details

2.1. Film deposition

An industrial-scale CemeCon AG (CC800/9) magnetron sputtering system is used for the deposition of $\text{Ti}_{1-x}\text{Al}_x\text{B}_y$ film alloys. The rectangular TiB_2 and AlB_2 targets with dimensions 8.8×50 cm² (99.7 % purity, provided by PLANSEE Composite Materials GmbH, Germany) are used. A deposition pressure is maintained at 0.4 Pa with a constant Ar gas flow of 400 sccm. Si(001) substrates, 2.0×1.0 cm², are cleaned in an ultrasonic bath using first acetone and then isopropanol alcohol and subsequently blow-dried with N_2 gas before being inserted into the deposition chamber. As-prepared substrates are coated with a 40-nm-thick Cr buffer layer to increase the adhesion between substrate and $\text{Ti}_{1-x}\text{Al}_x\text{B}_y$ layers, as commonly practiced [36]. A schematic illustration of the deposition setup is included in the [supplementary file](#) (cf. Fig. S1). Two resistance heaters, each powered to 2 kW, are used during the 1 h heating phase, resulting in the substrate temperature T_s of 120 °C, i.e., sufficiently high to desorb water vapor from chamber walls efficiently. After that, the heaters are turned off, and the system can cool down to 65 °C for another hour, resulting in a base pressure of 0.3 mPa. No external heating is applied to the substrate during film growth. T_s reaches the maximum of 180 °C (TiB_2 -HiPIMS/ AlB_2 -DCMS) and 160 °C (AlB_2 -HiPIMS/ TiB_2 -DCMS) due to plasma heating.

All $\text{Ti}_{1-x}\text{Al}_x\text{B}_y$ thin films are grown using hybrid HiPIMS/DCMS co-sputtering with one magnetron operated in HiPIMS mode and the other as a conventional DC source. Film elemental compositions are then controlled by varying the average power applied to the dc magnetron, P_{DCMS} , while the HiPIMS average power, P_{HiPIMS} , is constant. Two series of films are deposited. In the first set, the TiB_2 target is powered by HiPIMS, and the AlB_2 target works in DCMS mode (TiB_2 -HiPIMS/ AlB_2 -DCMS). $P_{\text{HiPIMS}} = 2.4$ kW, the duty cycle is 2.5 % with a HiPIMS pulse on-time, $\tau_{\text{HiPIMS}} = 50$ μ s, and the frequency, $f = 500$ Hz (cf. Fig. S2(a)-(b)). P_{DCMS} (AlB_2 target) varies from 1.0 to 5.0 kW (in steps of 1 kW), resulting in films with $0.36 \leq x \leq 0.74$ and $1.81 \leq y \leq 1.93$. The targets' positions are then switched for the second set of experiments (AlB_2 -HiPIMS/ TiB_2 -DCMS). In this configuration, $P_{\text{HiPIMS}} = 2$ kW (1.5 % duty cycle, and $\tau_{\text{HiPIMS}} = 30$ μ s) (cf. Fig. S2(c)-(d)), while P_{DCMS} (TiB_2 target)

ranges from 1.0 to 5.0 kW yielding films with $0.4 \leq x \leq 0.76$ and $1.92 \leq y \leq 2.03$. The deposition rate during AlB_2 -HiPIMS/ TiB_2 -DCMS growth decreases from 37 nm/min. with $x = 0.4$ to 19 nm/min. with $x = 0.74$. In the reversed target configuration the corresponding numbers vary between 18 nm/min. for $x = 0.36$ and 48 nm/min. for $x = 0.76$. The deposition time is varied from 40 to 95 min. in order to obtain films with comparable thickness in the range 1.7–1.9 μm .

A pulsed negative substrate bias V_s with the amplitude of 80 V is applied in synchronous with HiPIMS pulses. The V_s offset with respect to the HiPIMS cathode pulse is 30 μs , while the bias duration is 100- μs . To reduce the Ar^+ ions incorporation in the films, the substrate remains at a floating potential, $V_f \sim 16$ V, between the consecutive HiPIMS pulses.

Reference AlB_y (AlB_2 -DCMS) and TiB_y (TiB_2 -DCMS) layers are deposited at the $V_f \sim 16$ V, with the $P_{\text{DCMS}} = 5$ kW, corresponding to the current density of 0.03 A/cm^2 . The AlB_2 -HiPIMS and TiB_2 -HiPIMS depositions are conducted with a pulsed substrate bias, $V_s = 80$ V, and all other parameters are the same as during hybrid HiPIMS/DCMS co-sputtering. AlB_2 -DCMS/ TiB_2 -DCMS ($P_{\text{DCMS}} = 5.0/1.0$ kW and $1.0/5.0$ kW) depositions with $V_s = 80$ V DC bias are also carried out.

2.2. Characterization techniques

Ion mass spectrometry analyses are performed using an EQP 9 mass-energy analyzer (MEA) from Hidden Analytical to determine the composition and energy of ion fluxes incident at the growing film as a function of P_{DCMS} and target configuration. In these experiments, the spectrometer's grounded orifice (50 μm in diameter) is aligned parallel to the HiPIMS target surface. The 18 cm target-to-orifice length corresponds to the target/substrate distance during hybrid HiPIMS/DCMS co-sputtering to ensure that ion fluxes' intensities and time evolution represent that encountered during film growth. No additional heating is applied so that the temperature during analyses is similar to that during film growth. Time-resolved ion energy distribution functions (IEDFs) of the target (Ti^+ , Al^+ , B^+) and gas (Ar^+) ions are recorded with the 10 μs resolution starting from 0 and up to 200 μs after the ignition of the HiPIMS pulse. Each data point is registered during 500 consecutive HiPIMS pulses, giving a total acquisition time of 5 ms. All data were compensated for the charge/mass-dependent time-of-flight (TOF) through the instrument, as described in [42]. The ion energy, E_i , was scanned from $E_i = 1$ to 60 eV with the 1 eV step for all target ions and from 0 to 30 eV for Ar^+ . The data were also corrected for isotope abundance.

Quantitative elemental compositions of $\text{Ti}_{1-x}\text{Al}_x\text{B}_y$ alloy films are determined by time-of-flight elastic recoil detection analyses (ToF-ERDA) at the Tandem Accelerator Laboratory of Uppsala University. Recoils are created using a 36-MeV $^{127}\text{I}^{8+}$ beam incident at 67.5° with respect to the sample surface normal and detected at an angle of 45° with respect to the primary beam. Details of the measurement are given in [43].

The phase composition, crystal structure, lattice parameters, and orientation of film alloys are revealed using X-ray diffraction (XRD) θ -2 θ scans carried out in a Philips X'Pert X-ray diffractometer (using a point-focus $\text{Cu K}\alpha$ source with $\lambda = 0.15406$ nm). The substrate radius of curvature (R_s), required for measuring the residual stress, σ , of $\text{Ti}_{1-x}\text{Al}_x\text{B}_y$, is determined from a rocking-curve measurement of Si (004) reflections at room temperature, based on the Stoney equation and using a PANalytical Empyrean high-resolution X-ray diffractometer operated at 45 kV and 40 mA. The presented σ values are averaged results from measurements taken along several directions so that any error from uneven substrate bending is reduced.

X-ray photoelectron spectroscopy (XPS) core-level spectra are acquired with an Axis Ultra DLD instrument (Kratos Analytical, UK) with a base pressure lower than 1.5×10^{-7} Pa. The excitation source is a monochromatic $\text{Al-K}\alpha$ radiation ($h\nu = 1486.6$ eV). To minimize the effect of sputtering damage on core level spectra, mild etching with 0.5 keV Ar^+ ions incident at an angle of 70° from the surface normal is

applied [44,45]. Sample areas analyzed by XPS are $0.3 \times 0.7 \text{ mm}^2$ and located in the centre of $3 \times 3 \text{ mm}^2$ ion-etched regions. The Ti 2p, Al 2p, and B 1s spectra are charge-referenced to the Fermi edge cut-off at 0 eV [46].

The morphology and thicknesses of the thin films are assessed from fracture cross-section images captured by Zeiss Sigma 300 scanning electron microscopy (SEM) with an acceleration voltage of 3 kV and a working distance of 4.5 mm. Detailed microstructure studies of the $\text{Ti}_{1-x}\text{Al}_x\text{B}_y$ films are made by cross-sectional transmission electron microscopy (XTEM) and selective area electron diffraction (SAED) using an FEI Tecnai G2 microscope operated at 200 kV. TEM specimens are prepared by the traditional "sandwich" approach, which includes sample cutting, gluing, and polishing followed by Ar^+ ion milling at 4 keV and 6° angle from both sides in a Gatan precision ion polishing system. Ultimately, low-energy milling is applied at 1 keV for 30 min to reduce surface damage.

The NanoTester Vantage Alpha by Micro Materials, Ltd. (Wrexham, Wales) equipped with a diamond Berkovich probe is used to measure nanoindentation hardness H and reduced Young's modulus vs. film composition for $\text{Ti}_{1-x}\text{Al}_x\text{B}_y$. Depth sensing indentations are acquired with a constant load of 30 mN during a dwell period of 5 s, yielding indentation depths $< 10\%$ of the total film thicknesses. A Poisson ratio in between 0.11 (TiB_2) and 0.27 (AlB_2) weighted by the x composition together with a Poisson ratio of 0.07 and Young's modulus of 1141 GPa for a diamond indenter are used for the calculation of the Young's modulus, E , from the reduced Young's modulus [32]. The H and E values are then calculated following the method of Oliver and Pharr, considering elastic unloading part of the generated load-displacement curve. Square grids with 25 indents (separated by 50 μm each) specified the given standard deviation errors.

Air-annealing experiments are performed at the temperature $T_a = 800^\circ\text{C}$ for 1.0 h, using a furnace from MTI Corporation (GSL-1100 \times -S). The heating rate during oxidation process is set at 10°C/min , and the specimens are cooled to room temperature by turning off the furnace.

3. Results

3.1. Ion irradiation during hybrid HiPIMS/DCMS co-sputtering

Time-resolved Ti^+ , Al^+ , B^+ , and Ar^+ ion energy distribution functions (IEDFs) recorded at the substrate plane with a 20 μs resolution during hybrid AlB_2 -HiPIMS/ TiB_2 -DCMS and TiB_2 -HiPIMS/ AlB_2 -DCMS co-sputtering are plotted in Figs. 1 and 2, respectively. Results are shown for two extreme values of the DCMS power, $P_{\text{DCMS}} = 1.0$ and 5.0 kW.

During AlB_2 -HiPIMS/ TiB_2 -DCMS, both Al^+ and B^+ IEDFs initially ($40 \leq t \leq 80 \mu\text{s}$, in which $t = 0 \mu\text{s}$ denotes the ignition of the HiPIMS cathode pulse), show intense and broad energy distributions that are often observed during HiPIMS and are explained by the formation of potential humps in the ionization zones [47,48] (Fig. 1(a-b), 1(e-f)). During this phase, the average Al^+ and B^+ ion energies reach a maximum of ~ 15 eV, while the energy tails extend to 60 eV (for Al^+) and beyond (for B^+). For $t > 100 \mu\text{s}$, IEDFs collapse into a low-energy peak indicative of thermalization. In the case of lower DCMS power, the thermalized peak is centred at 2–3 eV, while for $P_{\text{DCMS}} = 5$ kW, the peak forms first at 5 eV ($100 \leq t \leq 120 \mu\text{s}$) and then moves to 9 eV towards the end of the measured time window of 200 μs . Ti^+ IEDFs (Fig. 1(c)-(d)) reveal the presence of Ti ions. However, the integrated Ti^+ ion fluxes are approximately an order of magnitude lower than those of Al^+ and B^+ ions, which is expected for a Ti target operating in DCMS mode [49]. The Ti^+/Al^+ flux ratio varies from 0.06 with $P_{\text{DCMS}} = 1.0$ kW to 0.13 with $P_{\text{DCMS}} = 5.0$ kW. The Ti^+ IEDFs are initially centred at 10–12 eV. In the case of $P_{\text{DCMS}} = 1.0$ kW, Ti^+ IEDFs form a thermalized peak at 2 eV for $t \gtrsim 80 \mu\text{s}$, while with $P_{\text{DCMS}} = 5.0$ kW, the distributions collapse into a peak at 5 eV ($120 \leq t \leq 140 \mu\text{s}$) that then shifts to 8 eV ($180 \leq t \leq 200 \mu\text{s}$). Qualitatively, very similar time evolution is observed for Ar^+ IEDFs (Fig. 1(g)-(h)), however, the overall flux intensities are much

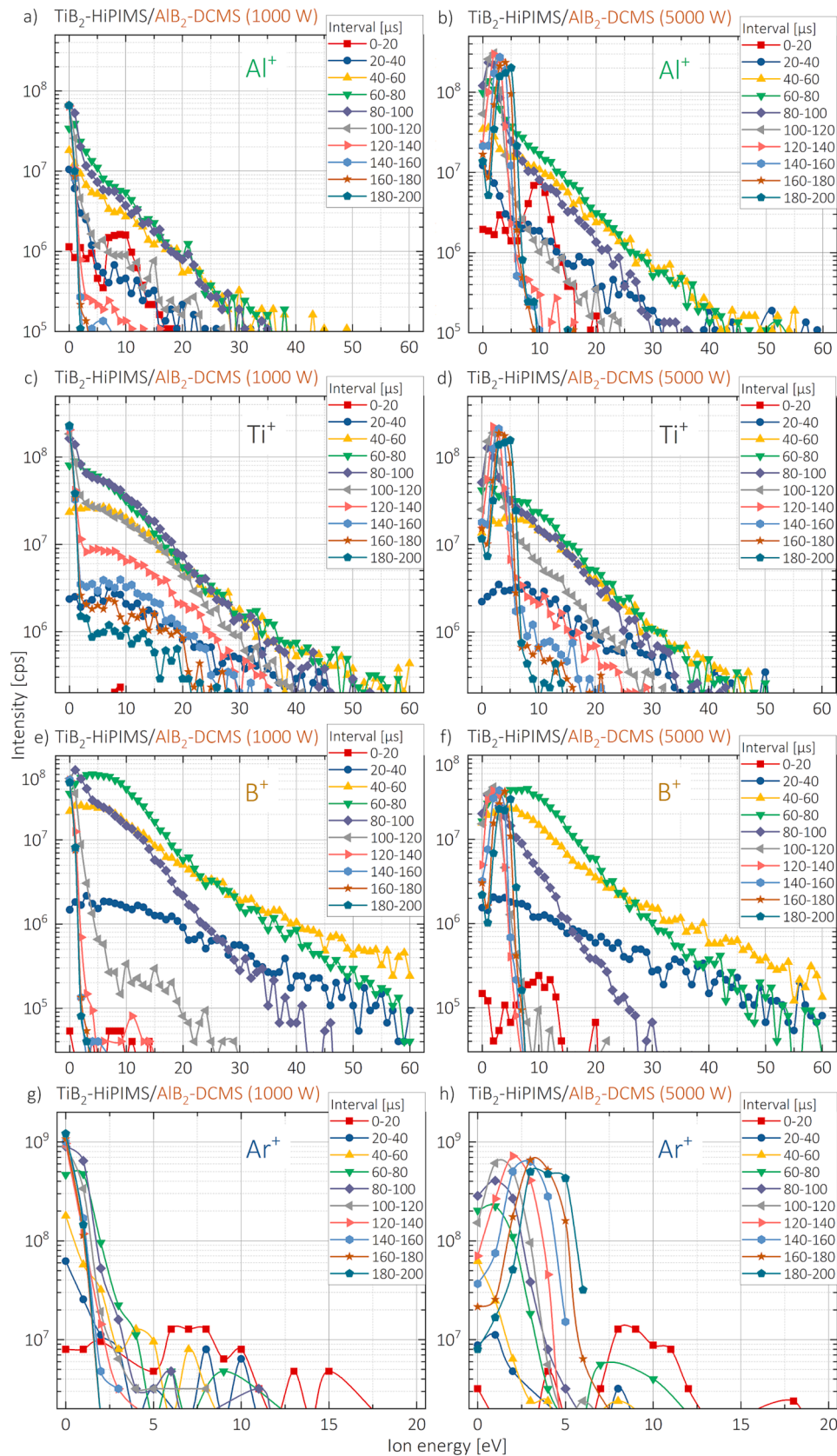


Fig. 1. Time-resolved Al^+ , Ti^+ , B^+ , Ar^+ IEDFs, recorded at the substrate position during hybrid TiB_2 -HiPIMS/ AlB_2 -DCMS sputtering with P_{DCMS} of 1.0 kW (left side), and 5.0 kW (right side). The IEDFs are shown for 20- μs intervals starting at $t = 0$ (pulse ignition) to 200 μs . The HiPIMS pulse length is 30 μs .

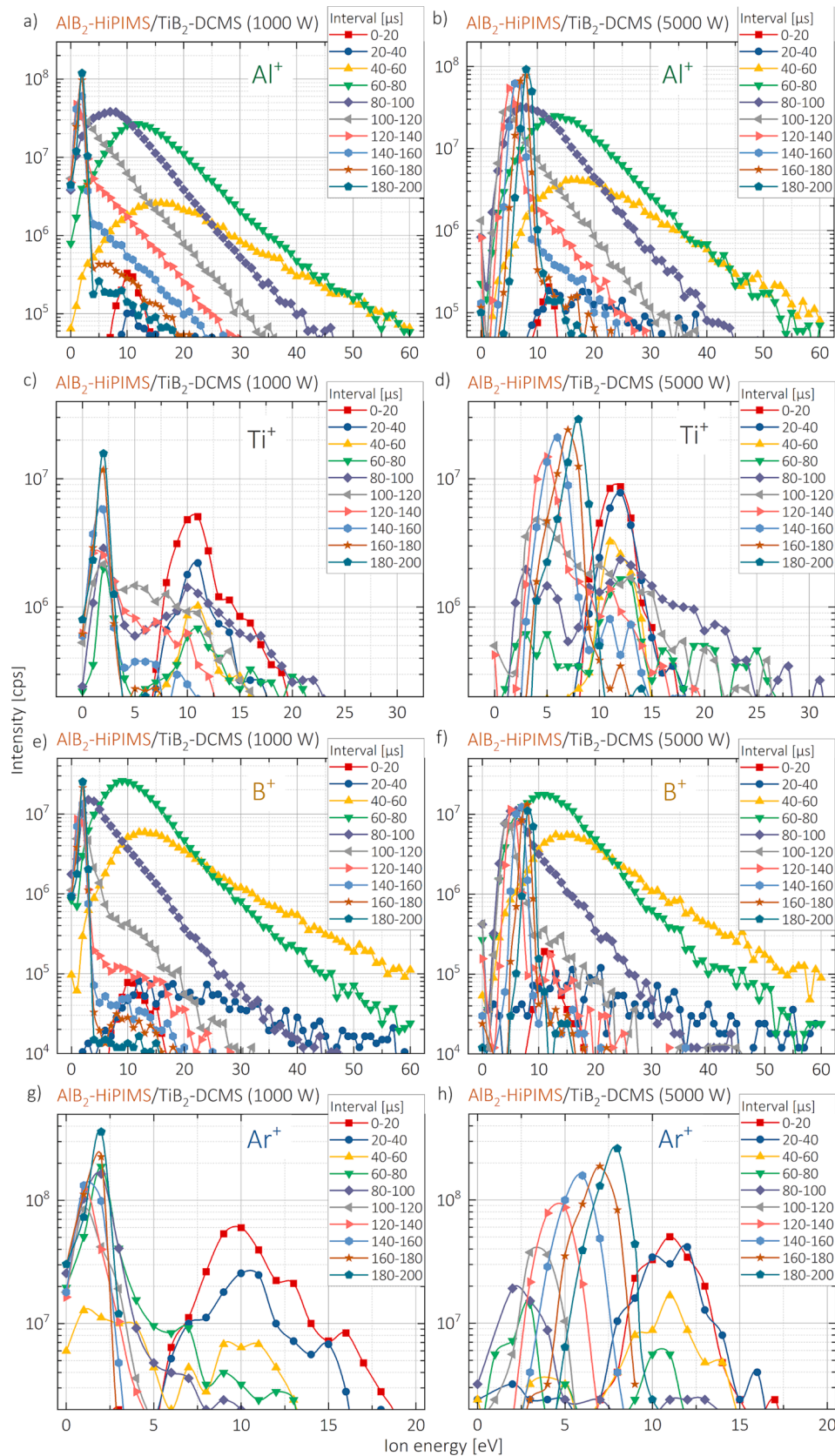


Fig. 2. Time-resolved Al^+ , Ti^+ , B^+ , Ar^+ IEDFs, recorded at the substrate position during hybrid AlB_2 -HiPIMS/ TiB_2 -DCMS sputtering with P_{DCMS} of 1.0 kW (left side), and 5.0 kW (right side). The IEDFs are shown for 20- μs intervals starting at $t = 0$ (pulse ignition) to 200 μs . The HiPIMS pulse length is 50 μs .

higher. For $P_{\text{DCMS}} = 1.0$ kW, the average Ar^+ ion energy is ~ 10 eV ($0 \leq t \leq 40$ μs) and decreases with time to ~ 2 eV as thermalization sets in. During hybrid co-sputtering at higher DCMS power, the thermalized peak forms first at 3 eV ($100 \leq t \leq 120$ μs) and eventually moves up to 8 eV ($180 \leq t \leq 200$ μs).

In the reversed target configuration, TiB_2 -HiPIMS/ AlB_2 -DCMS, Ti^+ ions have a high energy tails extending to ~ 40 eV, which is lower than the corresponding Al^+ distribution in the AlB_2 -HiPIMS/ TiB_2 -DCMS case, that reaches up to 60 eV. The B^+ ions ion energy distribution is similar in both cases. In distinct contrast to the AlB_2 -HiPIMS/ TiB_2 -DCMS co-sputtering, the ionization of the DCMS flux during TiB_2 -HiPIMS/ AlB_2 -DCMS is high, as evident from intense Al^+ IEDFs shown in Fig. 2(a)-(b). The Al^+/Ti^+ flux ratio shows a clear dependence on the DCMS power and varies from 0.19 with $P_{\text{DCMS}} = 1.0$ kW to 1.24 with $P_{\text{DCMS}} = 5.0$ kW. Thus, in the latter case, the Al^+ flux exceeds that of Ti^+ at the substrate, even though the Ti ionization for the HiPIMS-powered target must be significantly higher than the ionization in the Al flux ejected from the DCMS source. The thermalized Al^+ ions have energies very similar to those of Ti^+ and B^+ . Ar^+ IEDFs, shown in Fig. 1(g)-(h), reveal a much higher intensity of gas ions than during AlB_2 -HiPIMS/ TiB_2 -DCMS co-sputtering (Fig. 2(g)-(h)). The ion energies are, however, lower: the average Ar^+ ion energy is ~ 1 eV with $P_{\text{DCMS}} = 1.0$ kW, while for higher DCMS power, it varies from 1 eV ($60 \leq t \leq 80$ μs) to 4 eV ($180 \leq t \leq 200$ μs).

3.2. Elemental composition

The results of ERDA elemental analysis performed on all $\text{Ti}_{1-x}\text{Al}_x\text{B}_y$ alloy films grown in both TiB_2 -HiPIMS/ AlB_2 -DCMS and AlB_2 -HiPIMS/ TiB_2 -DCMS

TiB_2 -DCMS configurations are plotted as a function of DCMS power in Fig. 3(a) and 3(b), respectively. Compositions of TiB_y and AlB_y reference layers grown by (a) TiB_2 -HiPIMS ($V_s = 80$ V), (b) TiB_2 -DCMS ($P_{\text{DCMS}} = 5.0$ kW, $V_s = V_f$), (c) AlB_2 -HiPIMS ($V_s = 80$ V), and (d) AlB_2 -DCMS ($P_{\text{DCMS}} = 5.0$ kW, $V_s = V_f$) are also included. TiB_2 -HiPIMS/ AlB_2 -DCMS film series is slightly under-stoichiometric with y decreasing from 1.93 with $P_{\text{DCMS}} = 1.0$ kW to 1.81 with $P_{\text{DCMS}} = 5.0$ kW. x increases from 0.36 with $P_{\text{DCMS}} = 1.0$ kW to 0.76 with $P_{\text{DCMS}} = 5.0$ kW. In the case of AlB_2 -HiPIMS/ TiB_2 -DCMS growth, $\text{Ti}_{1-x}\text{Al}_x\text{B}_y$ films have compositions closer to B stoichiometry with y increasing from 1.86 with $P_{\text{DCMS}} = 1.0$ kW to 2.03 with $P_{\text{DCMS}} = 5.0$ kW. The Al metal fraction x decreases from 0.74 to 0.40 upon increasing P_{DCMS} from 1.0 to 5.0 kW. Thus, the x range is similar for both $\text{Ti}_{1-x}\text{Al}_x\text{B}_y$ film series. The reference TiB_y layers are overstoichiometric with $y = 2.46$ and 2.58 for TiB_2 -HiPIMS ($V_s = 80$ V) and TiB_2 -DCMS ($V_s = V_f$), respectively. Conversely, the AlB_y films obtained using AlB_2 -HiPIMS ($V_s = 80$ V) and AlB_2 -DCMS ($V_s = V_f$) are B-deficient with $y = 1.92$ and 1.85 , respectively.

In Fig. 3(c), the B/metal ratio y is plotted as a function of Al metal fraction x for all $\text{Ti}_{1-x}\text{Al}_x\text{B}_y$ layers. In addition, results are also shown for several films grown with AlB_2 -DCMS/ TiB_2 -DCMS target configuration and the 80-V DC bias: $\text{Ti}_{0.85}\text{Al}_{0.15}\text{B}_{2.67}$, $\text{Ti}_{0.7}\text{Al}_{0.3}\text{B}_{2.45}$, $\text{Ti}_{0.2}\text{Al}_{0.8}\text{B}_{2.14}$, and $\text{Ti}_{0.08}\text{Al}_{0.92}\text{B}_{1.97}$.

Irrespective of the growth mode, higher Al content is always associated with B deficiency. The dashed lines shown in Fig. 3(c) mark the expected $\text{Ti}_{1-x}\text{Al}_x\text{B}_y$ film compositions for the hybrid growth if the film stoichiometry would simply reflect the linear superposition of HiPIMS and DCMS fluxes (with the pulsed substrate bias, applied only during the HiPIMS phase). The endpoints ($x = 0$ and $x = 1$) correspond to the compositions of the respective reference binary layers: that is, for the

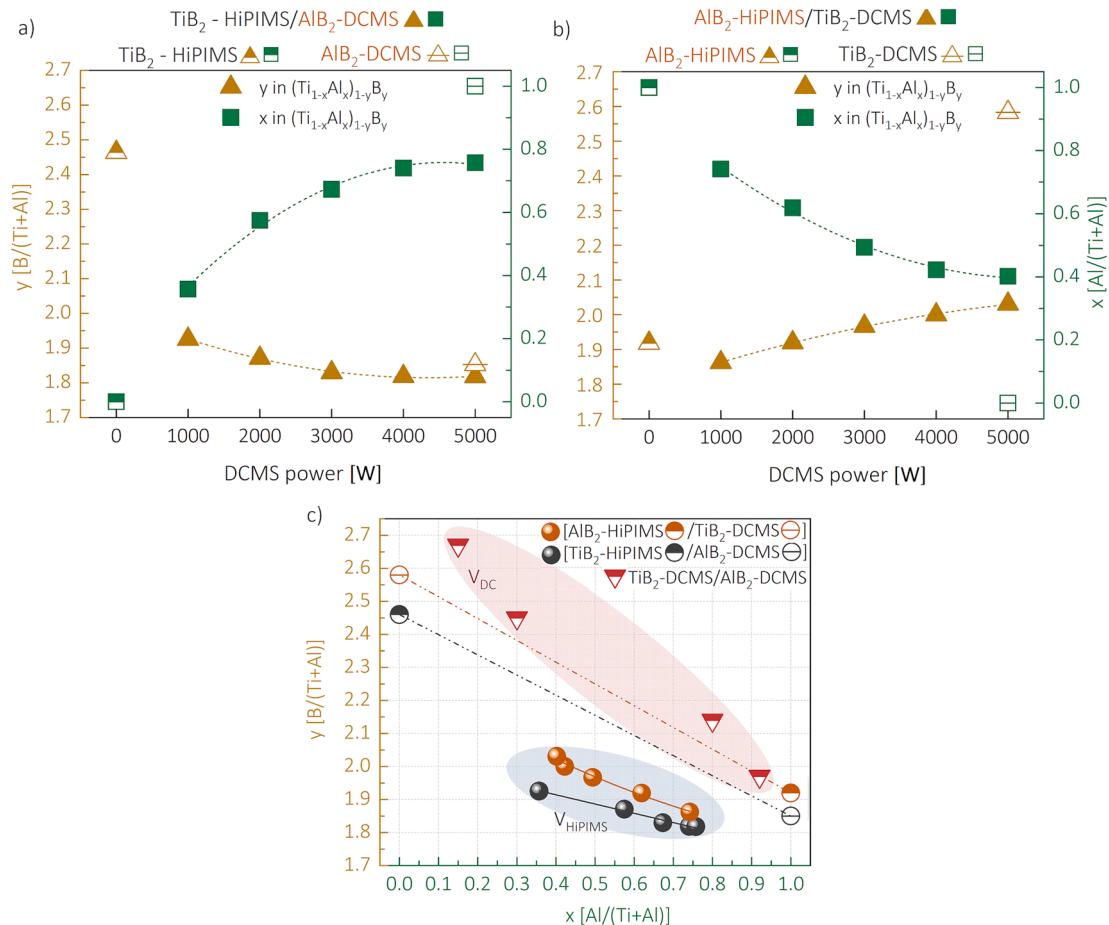


Fig. 3. $y = \text{B}/\text{metal}$ and $x = \text{Al}/(\text{Al} + \text{Ti})$ fractions obtained from ToF-ERDA for $\text{Ti}_{1-x}\text{Al}_x\text{B}_y$ films grown by (a) TiB_2 -HiPIMS/ AlB_2 -DCMS, and (b) AlB_2 -HiPIMS/ TiB_2 -DCMS. Results are plotted as a function of DCMS power P_{DCMS} . (c) a plot of y vs x showing results for the reference samples (see text for details).

TiB₂-HiPIMS/AlB₂-DCMS series, the reference films are TiB₂-HiPIMS grown with $V_s = 80$ V (TiB_{2.46}) and AlB₂-DCMS deposited at a floating bias (AlB_{1.85}), while for the AlB₂-HiPIMS/TiB₂-DCMS series, the references are AlB₂-HiPIMS deposited with $V_s = 80$ V (AlB_{1.92}) and TiB₂-DCMS grown with floating bias (TiB_{2.58}). For both hybrid target configurations, the B/metal ratios are significantly lower than what the linear superposition of HiPIMS plum and DCMS fluxes would suggest. Moreover, for a given x, the B/metal ratio is lower if the TiB₂ target operates in HiPIMS mode.

ERDA analyses also reveal that Ar concentration is below < 0.3 at.% in all Ti_{1-x}Al_xB_y films, while the measured oxygen content increases from 0.5 to 1.6 at.% with an increased Al content. The layers are hereafter referred to by their chemical composition obtained by ERDA.

3.3. XRD analysis

Fig. 4(a)-(b) shows XRD $\theta - 2\theta$ scans acquired from Ti_{1-x}Al_xB_y thin films grown using TiB₂-HiPIMS/AlB₂-DCMS and AlB₂-HiPIMS/TiB₂-DCMS configurations. Vertical dashed lines correspond to the reference powder-diffraction peak positions from AlB₂ [50] and TiB₂ [51]. A sharp S peak at 33.1° originates from the forbidden Si(002) reflection. Detected peaks are 001, 101, and 002 reflections corresponding to the hexagonal AlB₂-type crystal structure, revealing that all Ti_{1-x}Al_xB_y films are single-phase alloys. For TiB₂-HiPIMS/AlB₂-DCMS Ti_{1-x}Al_xB_y layers, the 001 reflections shift toward lower 2θ values with decreasing x, from 27.1° with x = 0.76 to 26.9° with x = 0.36. All these values are slightly lower than the corresponding 001 AlB₂ reference peak positions, thus revealing that films are in a compressive stress state. The preferred orientation evolves from 001 with x = 0.36 to 101 with x = 0.76. Detailed analysis of this trend is, however, complicated by the inherent column tilt induced by the co-sputtering geometry (cf. Fig. S1). Layers grown in the reversed target arrangement, AlB₂-HiPIMS/TiB₂-DCMS, are also single-phase. Similarly, 001 peaks are shifted toward higher 2θ values, which reveals a compressive stress state.

Hexagonal structure Ti_{1-x}Al_xB_y alloy lattice parameter c(x), calculated from the 001 and 002 reflections, is plotted in Fig. 4(c) for co-sputtered films in both hybrid configurations, TiB₂-HiPIMS/AlB₂-DCMS and AlB₂-HiPIMS/TiB₂-DCMS. The theoretical values calculated by density functional theory methods for single-phase hexagonal Ti_{1-x}Al_xB₂ films are included for comparison [32]. The arrangement of targets has a distinct effect on the c(x) plot. For TiB₂-HiPIMS/AlB₂-DCMS Ti_{1-x}Al_xB_y films, c decreases from 3.315 Å with x = 0.36 to 3.295 Å with x = 0.74. The AlB₂-HiPIMS/TiB₂-DCMS films show an opposite trend with c(x) increasing from 3.283 with x = 0.4 to 3.318 Å with x = 0.74.

3.4. Chemical bonding analysis

Ti 2p, B 1 s, and Al 2p XPS spectra recorded from the Ti_{1-x}Al_xB_y films grown with TiB₂-HiPIMS/AlB₂-DCMS and AlB₂-HiPIMS/TiB₂-DCMS are shown in Fig. 5. The Ti 2p core-level spectra consist of spin-split 2p_{3/2}-2p_{1/2} doublets. The Ti 2p_{3/2} peak is detected at 454.5 ± 0.1 eV irrespective of x and the target configuration used, in agreement with previous reports [35].

The B1s spectra reveal a single peak at 187.8 ± 0.1 eV from B in a diboride lattice. The variation in the B/metal ratio from 1.81 to 2.03 (cf. Fig. 3c) does not give rise to any additional contributions, in agreement with earlier reports [32].

Al 2p core-level spectra from TiB₂-HiPIMS/AlB₂-DCMS Ti_{1-x}Al_xB_y exhibit a single peak assigned to Al in the diboride lattice [35]. The position of that peak is 74.2 ± 0.1 eV independent of x. In the film with the highest Al content x = 0.76, an additional peak appears at 73.1 eV, which is commonly assigned to metallic Al bonds [32]. A comparison to Al 2p spectra recorded from as-deposited samples with oxidized surfaces (not shown) reveals a much lower intensity of that peak, indicating that the majority of metallic Al forms during Ar⁺ etching. Al 2p spectrum

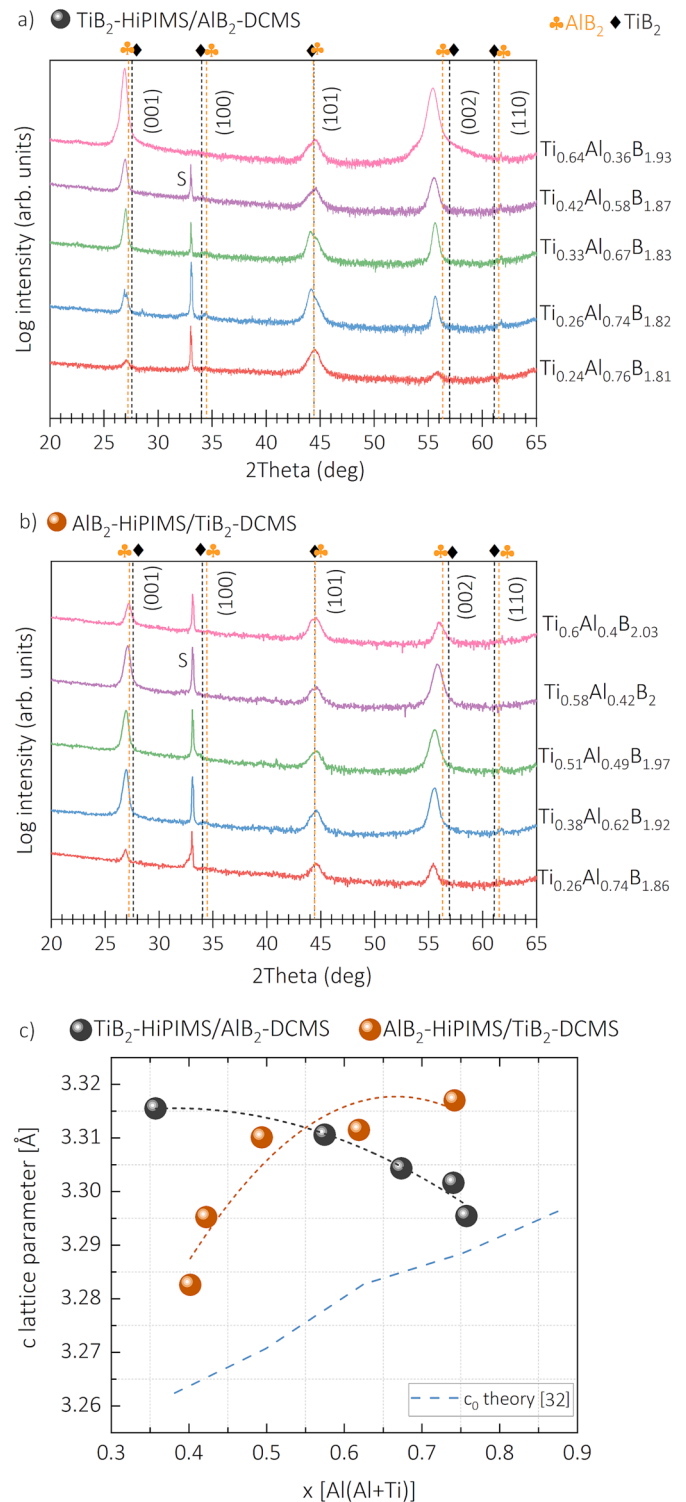


Fig. 4. XRD θ - 2θ scans for Ti_{1-x}Al_xB_y films deposited with (a) TiB₂-HiPIMS/AlB₂-DCMS, and (b) AlB₂-HiPIMS/TiB₂-DCMS configurations. Vertical dashed lines indicate positions of reference TiB₂ and AlB₂ reflections, while the peak at 33.1° arises from forbidden Si(001) substrate reflection. (c) c-lattice parameter plotted as a function of x. Calculated values [32] are shown for comparison.

from the latter sample also contains a small shoulder close to 75.4 eV, suggesting a residual Al oxide. The latter seems typical for TiB₂-HiPIMS/AlB₂-DCMS films with higher x, in agreement with the ToF-ERDA compositional analysis, which shows higher O content in all the Al-rich thin films. The Al 2p peak is also detected at the same binding

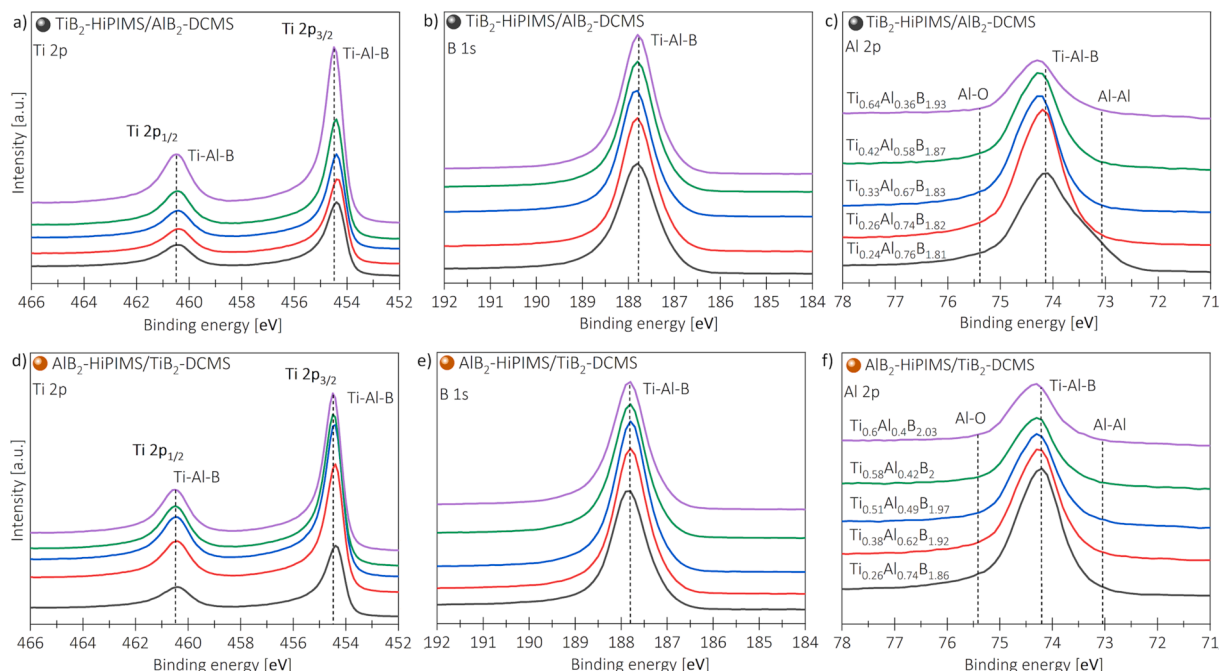


Fig. 5. Ti 2p, B 1 s, and Al 2p XPS core-level spectra acquired from the sputter-etched $Ti_{1-x}Al_xB_y$ film alloys corresponding to the hybrid (a-c) TiB_2 -HiPIMS/ AlB_2 -DCMS and (d-f) AlB_2 -HiPIMS/ TiB_2 -DCMS configuration.

energy in the AlB_2 -HiPIMS/ TiB_2 -DCMS $Ti_{1-x}Al_xB_y$.

3.5. Film morphology

The cross-sectional SEM images acquired from the TiB_2 -HiPIMS/ AlB_2 -DCMS and AlB_2 -HiPIMS/ TiB_2 -DCMS samples are shown in Fig. 6. Films from both series appear fully dense with smooth top surfaces. The cathode ion irradiation during hybrid co-sputtering is apparently sufficient to reduce surface roughening, faceting, associated atomic shadowing, and formation of voids, which are typical for such low deposition temperatures. The Ti-rich TiB_2 -HiPIMS/ AlB_2 -DCMS films with $x \leq 0.58$ exhibit dense and crystalline structures composed of fine nanograins elongated in the growth direction, whose size increases along film thickness. For the three other Al-rich films, competitive growth in which featureless (glassy) domains, free of porosity, form an inner layer up to a thickness of 450 ± 150 nm.

$Ti_{1-x}Al_xB_y$ film alloys with extreme x and y values from both series

are chosen for XTEM studies. Fig. 7 presents XTEM images from a) $Ti_{0.64}Al_{0.36}B_{1.93}$ and b) $Ti_{0.24}Al_{0.76}B_{1.81}$, TiB_2 -HiPIMS/ AlB_2 -DCMS film, while results for films grown in AlB_2 -HiPIMS/ TiB_2 -DCMS mode are depicted in panels c) $Ti_{0.26}Al_{0.74}B_{1.86}$ and d) $Ti_{0.6}Al_{0.4}B_{2.03}$. All four micrographs (taken from the area near the top surface of the thin films) reveal a dense columnar nanostructure. A distinct speckle contrast in all grains indicates, in turn, residual ion irradiation damage with local strain.

The TiB_2 -HiPIMS/ AlB_2 -DCMS $Ti_{0.64}Al_{0.36}B_{1.93}$ and $Ti_{0.24}Al_{0.76}B_{1.81}$ layers exhibit distinct columnar structures with a $\sim 20 \pm 10$ nm width, 40 ± 10 nm tall. The lower-Al $Ti_{0.64}Al_{0.36}B_{1.93}$ film has a fibrous structure with arc-shaped components from preferred 001 crystallographic orientation, (see SAED inset a). Full rings in the electron diffraction pattern overlapped with visible dark diffraction spots (inset b), suggests rather more randomly-oriented nanocrystallites forming in $Ti_{0.24}Al_{0.76}B_{1.81}$. The SAED patterns from all TiB_2 -HiPIMS/ AlB_2 -DCMS film alloys correspond to a single-solid solution hexagonal phase,

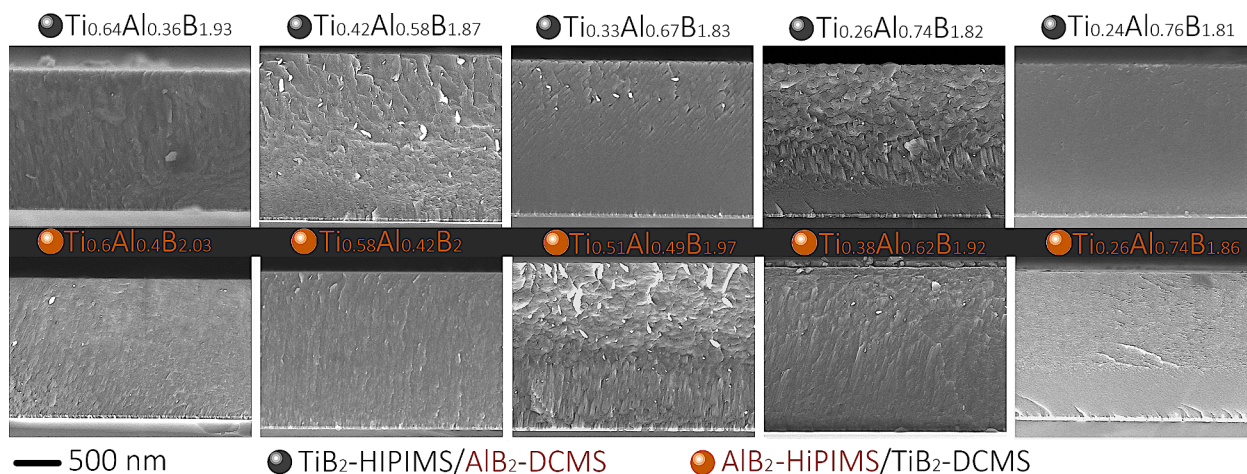


Fig. 6. Cross-sectional SEM (XSEM) images from $Ti_{1-x}Al_xB_y$ layers deposited by TiB_2 -HiPIMS/ AlB_2 -DCMS (on top) and AlB_2 -HiPIMS/ TiB_2 -DCMS (at the bottom). The Al fraction increases from left to right.

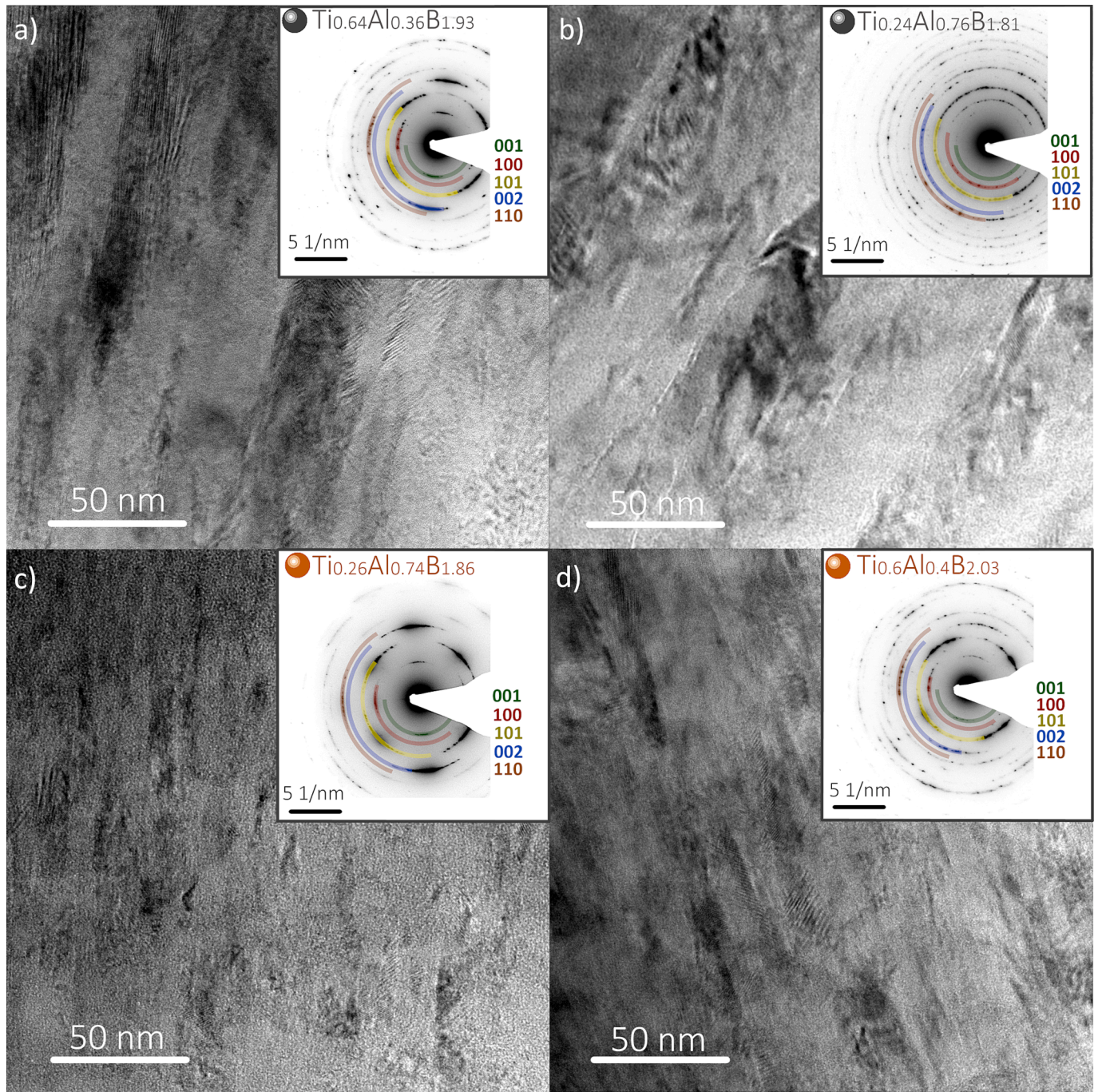


Fig. 7. (a) XTEM images along with the corresponding SAED patterns acquired from the middle portions of $Ti_{1-x}Al_xB_y$ films: (a) $Ti_{0.64}Al_{0.36}B_{1.93}$ (TiB_2 -HiPIMS/ AlB_2 -DCMS), (b) $Ti_{0.24}Al_{0.76}B_{1.81}$ (TiB_2 -HiPIMS/ AlB_2 -DCMS), (c) $Ti_{0.26}Al_{0.74}B_{1.86}$ (AlB_2 -HiPIMS/ TiB_2 -DCMS), and (d) $Ti_{0.6}Al_{0.4}B_{2.03}$ (AlB_2 -HiPIMS/ TiB_2 -DCMS).

irrespective of x .

XTEM images of the AlB_2 -HiPIMS/ TiB_2 -DCMS $Ti_{0.26}Al_{0.74}B_{1.86}$ and $Ti_{0.6}Al_{0.4}B_{2.03}$ films reveal a highly dense microstructures with fine columns, 10 ± 5 nm in-wide, and 25 ± 10 nm tall. A nanocrystalline structure with shared 001/101 (inset c)) and pure 101 texture (inset d)) in the growth direction can be fairly distinguished. The absence of diffraction from other phases shows that the AlB_2 -HiPIMS/ TiB_2 -DCMS layers, apart from the single-phase hexagonal $Ti_{1-x}Al_xB_y$ lattice, have a similar phase composition to that the TiB_2 -HiPIMS/ AlB_2 -DCMS films.

Detailed microstructure analysis of the Al-rich AlB_2 -HiPIMS/ TiB_2 -DCMS $Ti_{0.26}Al_{0.74}B_{1.86}$ and TiB_2 -HiPIMS/ AlB_2 -DCMS $Ti_{0.24}Al_{0.76}B_{1.81}$ samples shown in Fig. S3 confirm competitive film growth, in which the strongly disordered and amorphous-rich zones, start to be dominating

from the early stage of deposition. In the steady-state (corresponding to thickness larger than 450 ± 150 nm) the growth of Al-rich films is followed by fibrous (TiB_2 -HiPIMS/ AlB_2 -DCMS $Ti_{0.24}Al_{0.76}B_{1.81}$) or equiaxed crystalline (AlB_2 -HiPIMS/ TiB_2 -DCMS $Ti_{0.26}Al_{0.74}B_{1.86}$) structure. The transition from amorphous to nanocrystalline growth mode is induced by plasma heating.

3.6. Residual stress

The residual stresses, σ , for TiB_2 -HiPIMS/ AlB_2 -DCMS and AlB_2 -HiPIMS/ TiB_2 -DCMS film series are plotted as a function of x and y in Fig. 8(a) and 8(b), respectively. A clear trend is observed for the TiB_2 -HiPIMS/ AlB_2 -DCMS films: σ decreases with increasing Al content from

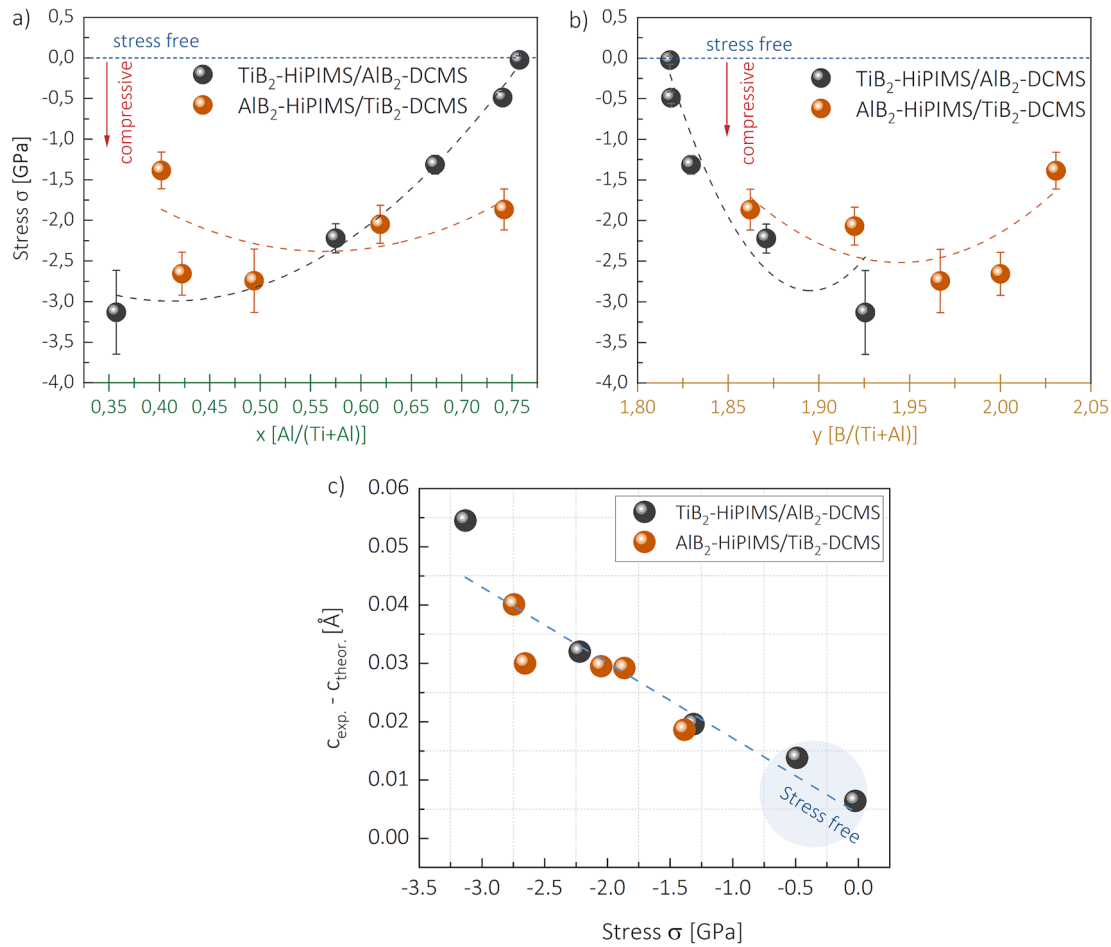


Fig. 8. Residual stress σ measured by the substrate curvature method for $\text{Ti}_{1-x}\text{Al}_x\text{B}_y$ films grown by the hybrid HiPIMS/DCMS plotted as a function of (a) $x = \text{Al}/(\text{Ti} + \text{Al})$, and (b) $y = \text{B}/(\text{Ti} + \text{Al})$. (c) difference between the measured and DFT-calculated [32] c-lattice parameter ($c_{\text{exp}} - c_{\text{theor}}$) plotted as a function of film stress state.

-3.2 ± 0.4 GPa with $x = 0.36$ to -0.03 ± 0.02 GPa with $x = 0.76$. x and y are correlated in this film series (cf. Fig. 3(c)), and the $\sigma(x)$ translates into an increase in compressive stress with increasing B (see Fig. 8(b)) as well as decreasing Al content (cf. Fig. S4). In contrast, no straightforward dependence of the residual stress on x or y is observed for AlB_2 -HiPIMS/ TiB_2 -DCMS film alloys. In this case, σ values vary in the range from -1.4 ± 0.2 to -2.8 ± 0.3 GPa.

Fig. 8(c) presents that for all $\text{Ti}_{1-x}\text{Al}_x\text{B}_y$ films, there is a correlation between the residual lattice stress and the deviation of the c lattice parameter from the theoretically predicted value.

3.7. Nanoindentation hardness and elastic moduli

The nanoindentation hardness H of TiB_2 -HiPIMS/ AlB_2 -DCMS and AlB_2 -HiPIMS/ TiB_2 -DCMS films is plotted as a function of x and y in Fig. 9 (a) and 9(d), respectively. For TiB_2 -HiPIMS/ AlB_2 -DCMS layers, H reaches a maximum value of 43.1 ± 2.6 GPa with $x = 0.36$ (and $y = 1.93$) and gradually decreases with increasing Al content to 37.6 ± 2.7 , 34.3 ± 2.3 , and 30.7 ± 2.1 GPa with $x = 0.57$, 0.67 , and 0.74 , respectively. The lowest value of 20.0 ± 1.2 GPa is obtained for the film with $x = 0.76$ and $y = 1.81$. A decrease in hardness with increasing x also occurs for AlB_2 -HiPIMS/ TiB_2 -DCMS layers. In the latter case, $H = 46.0 \pm 2.5$ GPa with $x = 0.4$ ($y = 2.03$) and decreases to 44.4 ± 3.5 , 44.1 ± 2.5 , and 37.6 ± 2.1 GPa with $x = 0.42$, 0.49 , and 0.62 , respectively. Even the film with the highest Al content ($x = 0.74$) has a high H value of 32.8 ± 1.7 GPa.

The same sets of data replotted as a function of the B/metal ratio (cf. Fig. 9(d)) reveal that H increases with increasing B content, irrespective

of the target configuration performed. The increase is particularly apparent for $1.80 < y < 1.93$ and saturates for $y \geq 1.93$. All $\text{Ti}_{1-x}\text{Al}_x\text{B}_y$ layers that fall into the latter category are superhard ($H > 40$ GPa).

Nanoindentation elastic moduli E of TiB_2 -HiPIMS/ AlB_2 -DCMS and AlB_2 -HiPIMS/ TiB_2 -DCMS layers are plotted as a function of x and y in Fig. 9(b) and 9(e), respectively. For TiB_2 -HiPIMS/ AlB_2 -DCMS layers, E reaches a maximum value of 433.0 ± 16.5 GPa with $x = 0.36$ (and $y = 1.93$) and gradually decreases with increasing Al content to 387.2 ± 12.6 , 366.8 ± 10 , and 338.8 ± 11.3 GPa with $x = 0.57$, 0.67 , and 0.74 , respectively. The lowest value of 298.2 ± 8.5 GPa is obtained for the film with $x = 0.76$ and $y = 1.81$. Moreover, a decrease in elastic moduli with increasing x is also observed for AlB_2 -HiPIMS/ TiB_2 -DCMS films. In this case, $E = 481.5 \pm 9.7$ GPa with $x = 0.4$ ($y = 2.03$) and decreases to 448.4 ± 10.3 , 442.4 ± 12.7 , and 379.6 ± 6.0 GPa with $x = 0.42$, 0.49 , and 0.62 , respectively. Similar to TiB_2 -HiPIMS/ AlB_2 -DCMS layers with the highest Al content, AlB_2 -HiPIMS/ TiB_2 -DCMS with $x = 0.74$ shows a slightly lower E value of 335.6 ± 8.6 GPa. The same sets of data replotted as a function of B/metal ratio (cf. Fig. 9(e)) reveal a linear increase in E with increasing y . The above results indicate that the elastic moduli for co-sputtered $\text{Ti}_{1-x}\text{Al}_x\text{B}_y$ films are a linear superposition of corresponding values for TiB_2 (580 GPa) and AlB_2 (250 GPa) [32].

The resistance to plastic deformation can be characterized by the H^3/E^2 ratio [52]. Hence, H^3/E^2 for both film series is plotted as a function of x and y in Fig. 9(c) and 9(f), respectively. H^3/E^2 values decrease with increasing Al content from 0.43 to 0.09 for the TiB_2 -HiPIMS/ AlB_2 -DCMS series and from 0.44 to 0.31 for films grown with AlB_2 -HiPIMS/ TiB_2 -DCMS. When plotted as a function of the B/metal ratio, H^3/E^2 values are found to increase with y and saturate for $y \geq 1.93$.

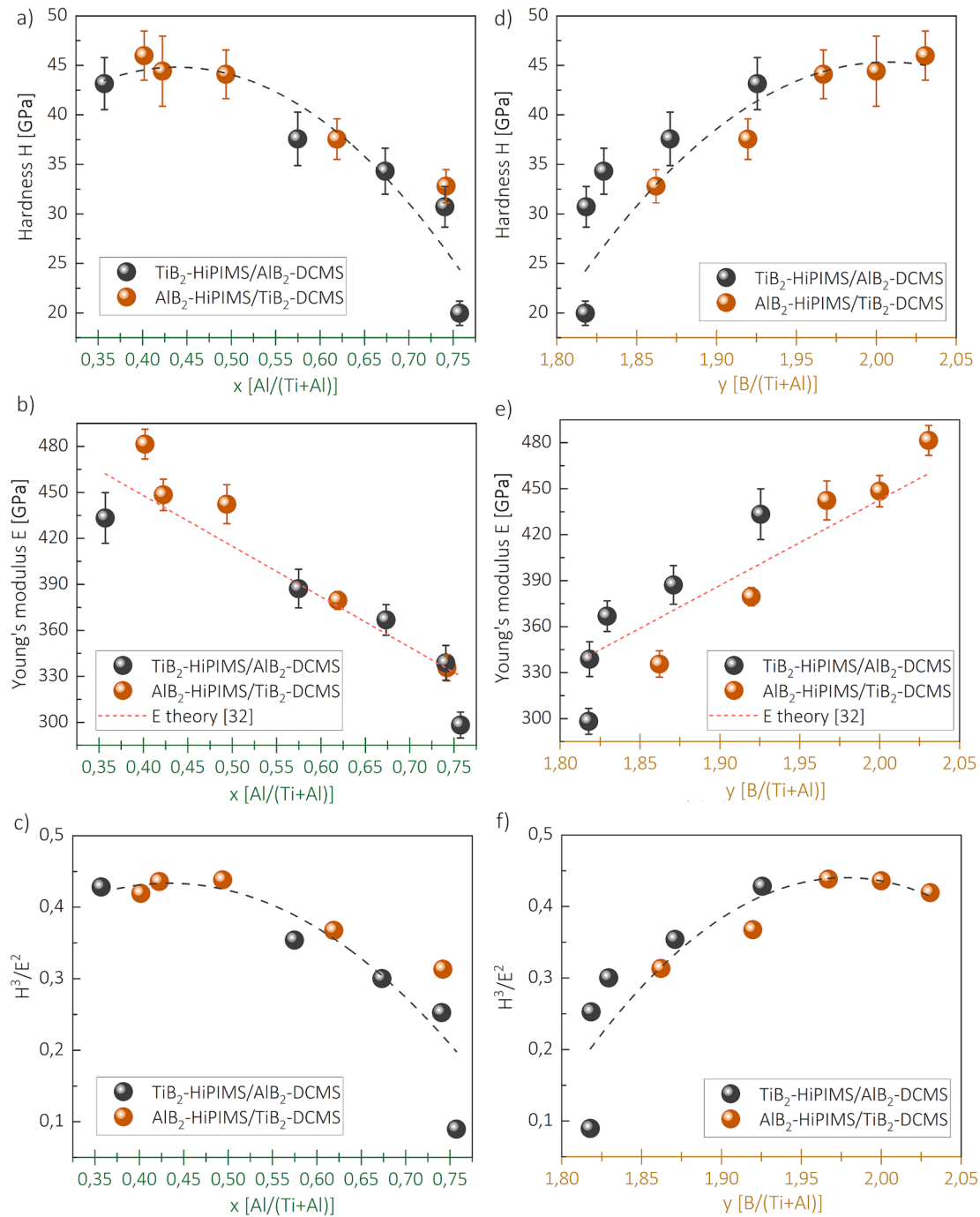


Fig. 9. Nanoindentation hardness, elastic moduli, and H^3/E^2 ratios for both series of $Ti_{1-x}Al_xB_y$ thin films deposited by the hybrid HiPIMS/DCMS methods. Results are shown as a function of (a-c) $x = Al/(Ti + Al)$, and (d-f) $y = B/(Ti + Al)$. E_{theory} plotted as a function of x . Calculated values [32] are shown for comparison.

3.8. Annealing in air

Fig. 10(a) and 10(b) show the XSEM-derived oxide scale thickness, d_{ox} , formed on top of TiB_2 -HiPIMS/ AlB_2 -DCMS and AlB_2 -HiPIMS/ TiB_2 -DCMS film alloys following 1 h long air annealing at 800 °C plotted as a function of x and y , respectively. The nanoindentation data, acquired before heat treatment, are also attached to determine which layers offer the best hardness and oxidation resistance combination.

Irrespective of growth mode, d_{ox} decreases with increasing Al content, from $\sim 705 \pm 140$ nm with $x = 0.36$ to $\sim 560 \pm 110$ nm with $x = 0.49$. This is followed by a steep increase in oxidation resistance for layers with $x \gtrsim 0.58$, which have oxide scale thickness lower than 180 nm. In the limit of Al content ($x = 0.74$ – 0.76), d_{ox} is as low as 45 ± 10

nm. Significantly, the gain in the oxidation resistance that takes place between $x = 0.5$ and $x = 0.58$ (d_{ox} reduced by a factor of $\times 3.1$) more than outweighs the $\sim 16\%$ loss in H . Hence, $Ti_{1-x}Al_xB_y$ films with $0.58 \leq x \leq 0.67$ represent the best system performance, with an average oxide scale thickness of 90–180 nm and hardness 34–38 GPa. If oxidation resistance is the primary concern, films with $x = 0.74$ provides even better performance with $d_{ox} = 45 \pm 10$ nm and H value exceeding 30 GPa.

4. Discussion

Detailed knowledge concerning the time evolution of ion fluxes incident at the growing film surface during hybrid HiPIMS/DCMS

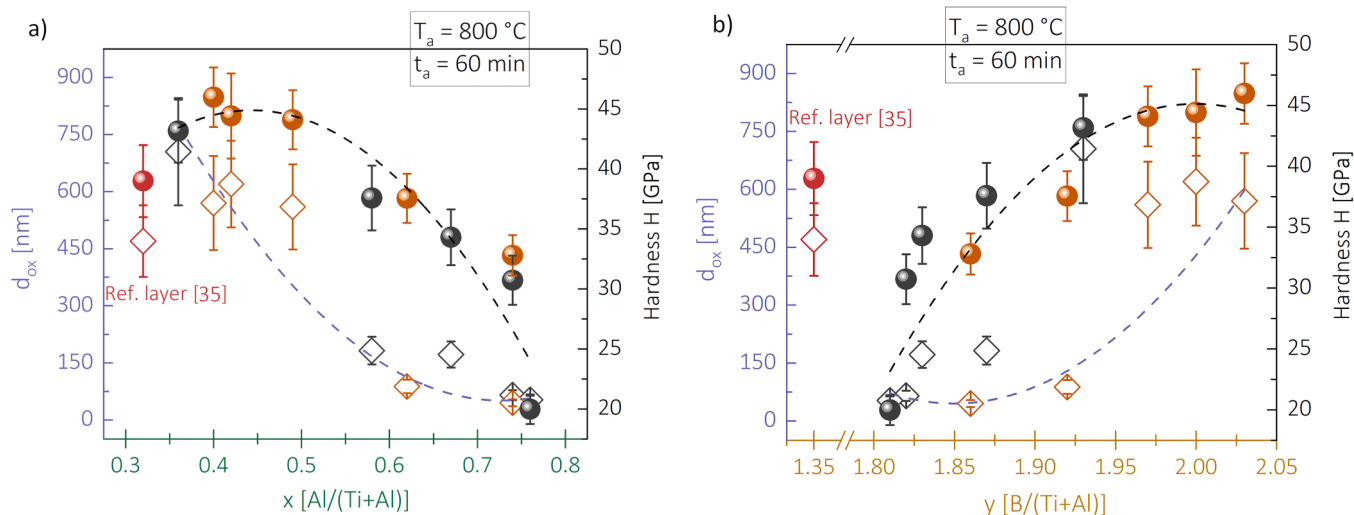


Fig. 10. The oxide scale thickness d_{ox} for the air-annealed $\text{Ti}_{1-x}\text{Al}_x\text{B}_y$ films ($T_a = 800\text{ }^{\circ}\text{C}$ for $t_a = 1.0\text{ h}$) plotted together with the nanoindentation hardness H of as-deposited films. Results are shown as a function of (a) $x = \text{Al}/(\text{Ti} + \text{Al})$, and (b) $y = \text{B}/(\text{Ti} + \text{Al})$.

growth is essential for understanding what film elemental composition forms.

As revealed by time-resolved IEDFs shown in Figs. 1 and 2, during TiB_2 -HiPIMS/ AlB_2 -DCMS co-sputtering, the average energies of metal ions from the HiPIMS target are lower. This is accompanied by higher Ar^+ fluxes. An explanation is offered by the different degree of Ar rarefaction between the two cases. The strongest gas rarefaction and, hence, lowest Ar^+/Me^+ ion ratio was reported if the HiPIMS pulse was terminated when the target current density $J_T(t)$ reached the maximum amplitude [53]. If the target current was instead allowed to decay after reaching its maximum value, the Ar refill subsequently increased the relative Ar^+ fluxes. The latter scenario is valid in TiB_2 -HiPIMS/ AlB_2 -DCMS experiments, in which case the target pulse is terminated at $t = 50\text{ }\mu\text{s}$, while the maximum $J_T(t)$ is reached at $t = 30\text{ }\mu\text{s}$ (cf. Fig. S2a). In contrast, for AlB_2 -HiPIMS/ TiB_2 -DCMS hybrid deposition, HiPIMS pulses are terminated at $t = 30\text{ }\mu\text{s}$, which coincides with the $J_T(t)$ maximum (cf. Fig. S2c). Moreover, operation in the AlB_2 -HiPIMS returns a nearly 60 % higher power-normalized deposition rate than the reverse TiB_2 -HiPIMS mode. Consequently, the Ar^+ fluxes are less intense in the former case, and ions originating from this HiPIMS target possess higher average energy.

Ion mass spectrometry analyses are conducted in the hybrid configuration, which allows to examine the effect of cross-interactions, with ionization in particular, between HiPIMS and DCMS plasmas. Interestingly, the ionization degree of the DCMS flux by HiPIMS plasma plume near the substrate plane strongly depends on which target, AlB_2 or TiB_2 , is operated in HiPIMS mode. Results presented in Figs. 1 and 2 reveal that the ionization of Al neutral fluxes from DCMS cathode during TiB_2 -HiPIMS/ AlB_2 -DCMS is much more efficient than the ionization of Ti neutrals in AlB_2 -HiPIMS/ TiB_2 -DCMS setup. Noteworthy, during the TiB_2 -HiPIMS/ AlB_2 -DCMS operation with $P_{\text{DCMS}} = 5.0\text{ kW}$, the Al^+ flux is higher than the Ti^+ flux, even though the Ti ionization at the target side must be much higher than that of Al. The difference in the first ionization potentials of sputtered metals explain this effect. During the metal phase of HiPIMS the electron temperature of the HiPIMS plume is truncated at the ionization potential of the dominant metal [54]. As the first ionization potential of Ti atoms ($\text{IP}_{\text{Ti}}^1 = 6.83\text{ eV}$) is higher than the first ionization potential of Al ($\text{IP}_{\text{Al}}^1 = 5.99\text{ eV}$), there are plenty of energetic electrons capable ion ionizing Al during TiB_2 -HiPIMS/ AlB_2 -DCMS (through the electron-impact ionization [55]), while there are no (or few) electrons capable of ionizing Ti if the reverse target configuration is used. The process is further facilitated by the condition that Al has a higher cross-section for electron collisions ($\sigma_{\text{Al}} = 1.5 \times 10^{-15}$)

compared to that of B and Ti atoms ($\sigma_{\text{B}} = 2.8 \times 10^{-16}$, and $\sigma_{\text{Ti}} = 5.6 \times 10^{-16}$) [56]. An additional mechanism that may be active to further enhance Al^+ content during TiB_2 -HiPIMS/ AlB_2 -DCMS is charge exchange collisions between Ti^+ and Al, that are energetically favored due to the difference in ionization potentials. Penning ionization due to metastable Ar^* ($3p^54s$) species with excitation energy varying from 11.55 eV to 11.83 eV [57] from the HiPIMS source can also be contributing after the HiPIMS pulse has been turned off [58].

It is clear from ERDA results (cf. Fig. 3(c)) that the B/metal ratio decreases with increasing Al for all $\text{Ti}_{1-x}\text{Al}_x\text{B}_y$ films, irrespective of what method and target configuration is used. This result suggests that a common factor, primarily the angular distribution of the sputtered species, plays a key role, independent of the ionization degree of sputter-ejected flux (which obviously differs substantially between different configurations engaged). Neidhardt et al. [59] presented computationally and experimentally that B is preferentially ejected along the surface normal while Ti is effectively emitted at higher angles. In line with that, Martynenko et al. [60] showed that the maximum Ti emission from the elemental target is at $\sim 30^\circ$ from the surface normal, whereas Al is emitted perpendicular to the target surface. Based on these results, one can thus expect that in the case of hybrid $\text{Ti}_{1-x}\text{Al}_x\text{B}_y$ growth, the off-axis metal flux decreases with increasing x , resulting in a decreasing B/metal ratio as it was already observed (cf. Fig. 3(c)).

For the hybrid HiPIMS/DCMS target configurations this asymmetry in the angular cosine distribution of Ti and Al will continue to play a role. Here, however, we have higher ionization probabilities for the metal atoms compared to boron, which lead to further increase of the metal component in the film alloys (lower y -values) as compared to the linear superposition of results obtained for reference diborides grown by pure HiPIMS and pure DCMS would suggest (see Fig. 3(c)). The lower y values measured if the TiB_2 target operates in HiPIMS mode can be explained by the enhanced ionization of the DCMS sputtered Al flux as demonstrated in Figs. 1 and 2, and as discussed above.

Results presented in Fig. 10 reveal a clear improvement in the high temperature oxidation resistance with increasing Al content. Irrespective of the growth mode used, the oxide scale thickness decreases more than 15 times upon increasing x from 0.36 to 0.74. The effect is preliminary attributed to the passivating properties of Al-containing oxides, in analogy to the TiAlN system [61]. $\text{Ti}_{1-x}\text{Al}_x\text{B}_y$ layers with $0.58 \leq x \leq 0.67$ offer, in turn, the best compromise between high-temperature oxidation resistance and mechanical properties with an average oxide scale thickness of 90–180 nm and a hardness of 34–38 GPa. If the oxidation resistance is of primary concern, diboride film with

$x = 0.74$ is the better choice with $d_{ox} = 45 \pm 10$ nm and H exceeding 30 GPa.

5. Conclusions

Hybrid HiPIMS/DCMS co-sputtering with AlB_2 and TiB_2 targets was used to grow $Ti_{1-x}Al_xB_y$ thin film alloys with $0.40 \leq x \leq 0.76$ and $1.81 \leq y \leq 2.03$. Two target configurations were explored: AlB_2 -HiPIMS/ TiB_2 -DCMS and TiB_2 -HiPIMS/ AlB_2 -DCMS. The substrate temperature during growth was lower than 180 °C with no external heating applied. Time-resolved ion mass spectrometry analyses, conducted at the substrate plane, revealed that the ionization of DCMS flux is highest during TiB_2 -HiPIMS/ AlB_2 -DCMS, which can be explained by the difference in the first ionization potentials of sputtered metal atoms and the different probability for electron-impact ionization.

The B/metal ratio in the single-phase $Ti_{1-x}Al_xB_y$ thin film alloys was observed to decrease with increasing x , irrespective of the target configuration used, because of difference between angular distributions of Ti and Al atoms emitted from TiB_2 and AlB_2 targets. Films grown with TiB_2 -HiPIMS/ AlB_2 -DCMS contained less atomic B for a given x . This effect is caused by higher metal-ion content in the plasma (due to the efficient cross-ionization) steered to the negatively-biased substrate to preserve plasma neutrality.

A significant improvement in high-temperature oxidation resistance of $Ti_{1-x}Al_xB_y$ films takes place with increasing Al content. The thickness of the oxide scale forming after 1 h anneal at 800 °C in air decreased more than 15 times upon increasing x from 0.36 to 0.74. $Ti_{1-x}Al_xB_y$ layers with $0.58 \leq x \leq 0.67$ offer an optimization between high-temperature oxidation resistance and mechanical strength with an average oxide scale thickness of 90–180 nm and hardness 34–38 GPa. If the oxidation resistance is of primary concern, AlB_2 -HiPIMS/ TiB_2 -DCMS $Ti_{1-x}Al_xB_y$ film with $x = 0.74$ is the best solution with $d_{ox} = 45 \pm 10$ nm and H exceeding 30 GPa.

CRediT authorship contribution statement

B. Wicher: Writing – review & editing, Writing – original draft, Visualization, Resources, Methodology, Investigation, Funding acquisition. **A.V. Pshyk:** Methodology, Investigation. **X. Li:** Methodology, Investigation. **B. Bakht:** Software, Investigation. **V. Rogoz:** Software, Methodology. **I. Petrov:** Writing – review & editing, Validation, Resources, Formal analysis. **L. Hultman:** Writing – review & editing, Supervision, Funding acquisition, Conceptualization. **G. Greczynski:** Writing – original draft, Writing – review & editing, Supervision, Funding acquisition, Conceptualization.

Declaration of competing interest

The authors declare that they have no known competing financial interests or personal relationships that could have appeared to influence the work reported in this paper.

Data availability

Data will be made available on request.

Acknowledgments

The authors gratefully acknowledge the financial support of the Swedish Research Council VR Grant 2018-03957 and 2021-00357, the Swedish Energy Agency under project 51201-1, the Åforsk Foundation Grant 22-4, the Knut and Alice Wallenberg Foundation Scholar Grant KAW2019.0290, the Olle Engqvist foundation grant 222-0053, and the Carl Tryggers Stiftelse contract CTS 20:150. Support from the Swedish Research Council VR-RFI (2019-00191) for the Accelerator based ion-technological center for the Tandem Accelerator Laboratory in

Uppsala University is acknowledged. We thank the Swedish Research Council and SSF for access to ARTEMIS, the Swedish National Infrastructure in Advanced Electron Microscopy (2021-00171 and RIF21-0026). This work was partially supported by the Wallenberg Initiative Materials Science for Sustainability (WISE) funded by the Knut and Alice Wallenberg Foundation. Bartosz Wicher is grateful to the Polish National Agency for Academic Exchange for support under the Bekker Programme (BPN/BEK/2021/1/00366/U/00001) and the Warsaw University of Technology within the Excellence Initiative: Research University, IDUB Mobility program (1820/74/Z09/2023).

Appendix A. Supplementary data

Supplementary data to this article can be found online at <https://doi.org/10.1016/j.matdes.2024.112727>.

References

- [1] Q. Wang, C. Liu, R. Yao, H. Zhu, X. Liu, M. Wang, Z. Chen, H. Wang, First-principles study on the stability and work function of low-index surfaces of TiB_2 , *Comput. Mater. Sci.* 172 (2020) 109356, <https://doi.org/10.1016/j.commatsci.2019.109356>.
- [2] B. Wicher, R. Chodun, M. Trzcinski, A. Lachowski, K. Nowakowska-Langier, S. H. Ibrahim, J. Jaroszewicz, M. Kubiś, E. Grzanka, K. Zdunek, Application of the plasma surface sintering conditions in the synthesis of ReB_2 -Ti targets employed for hard films deposition in magnetron sputtering technique, *Int. J. Refract. Met. Hard Mater.* 103 (2022) 105756, <https://doi.org/10.1016/j.jirmhm.2021.105756>.
- [3] V. Moraes, L. Zauner, T. Wojcik, M. Arndt, P. Polcik, H. Riedl, P.H. Mayrhofer, Thermally stable superhard diborides: An ab initio guided case study for V-W-diboride thin films, *Acta Mater.* 186 (2020) 487–493, <https://doi.org/10.1016/j.actamat.2020.01.014>.
- [4] I.I. Korobov, G.V. Kalinnikov, A.V. Ivanov, N.N. Dremova, R.A. Andrievski, S. P. Shilkin, Corrosion resistance of nanostructured films of titanium diboride in mineral acid solutions, *Prot. Met. Phys. Chem. Surfaces.* 52 (2016) 618–621, <https://doi.org/10.1134/S2070205116040171>.
- [5] B. Wicher, R. Chodun, M. Trzcinski, A. Lachowski, M. Kubiś, K. Nowakowska – Langier, K. Zdunek, Design of pulsed neon injection in the synthesis of W-B-C films using magnetron sputtering from a surface-sintered single powder cathode, *Thin Solid Films* 716 (2020) 138426, <https://doi.org/10.1016/j.tsf.2020.138426>.
- [6] H. Euchner, P.H. Mayrhofer, H. Riedl, F.F. Klimashin, A. Limbeck, P. Polcik, S. Kolozsvári, Solid solution hardening of vacancy stabilized $Ti_{1-x}B_2$, *Acta Mater.* 101 (2015) 55–61, <https://doi.org/10.1016/j.actamat.2015.08.048>.
- [7] C.M. Koller, R. Hollerweger, C. Sabitzer, R. Rachbauer, S. Kolozsvári, J. Paulitsch, P.H. Mayrhofer, Thermal stability and oxidation resistance of arc evaporated $TiAlN$, $TaAlN$, $TiAlTaN$, and $TiAlN/TaAlN$ coatings, *Surf. Coatings Technol.* 259 (2014) 599–607, <https://doi.org/10.1016/j.surfcoat.2014.10.024>.
- [8] M. Mikula, B. Grančić, V. Buršiková, A. Csuba, M. Držik, Š. Kavecký, A. Plecenik, P. Kús, Mechanical properties of superhard TiB_2 coatings prepared by DC magnetron sputtering, *Vacuum* 82 (2007) 278–281, <https://doi.org/10.1016/j.vacuum.2007.07.036>.
- [9] N. Schalk, J. Keckes, C. Czettl, M. Burghammer, M. Penoy, C. Michotte, C. Mitterer, Investigation of the origin of compressive residual stress in CVD TiB_2 hard coatings using synchrotron X-ray nanodiffraction, *Surf. Coatings Technol.* 258 (2014) 121–126, <https://doi.org/10.1016/j.surfcoat.2014.09.050>.
- [10] T. Glechner, O.E. Hudak, T. Wojcik, L. Haager, F. Bohrn, H. Hutter, O. Hunold, J. Ramm, S. Kolozsvári, E. Pitthan, D. Primetzhofer, H. Riedl, Influence of the non-metal species on the oxidation kinetics of Hf, HfN, HfC, and HfB_2 coatings, *Mater. Des.* 211 (2021) 110136, <https://doi.org/10.1016/j.matdes.2021.110136>.
- [11] P.H. Mayrhofer, C. Mitterer, J.G. Wen, J.E. Greene, I. Petrov, Self-organized nanocolumnar structure in superhard TiB_2 thin films, *Appl. Phys. Lett.* 86 (2005) 131909, <https://doi.org/10.1063/1.1887824>.
- [12] N. Nedfors, A. Mockute, J. Palisaitis, P.O.Å. Persson, L.-Å. Näslund, J. Rosen, Influence of pulse frequency and bias on microstructure and mechanical properties of TiB_2 coatings deposited by high power impulse magnetron sputtering, *Surf. Coatings Technol.* 304 (2016) 203–210, <https://doi.org/10.1016/j.surfcoat.2016.06.086>.
- [13] M. Mikula, B. Grančić, T. Roch, T. Plecenik, I. Vávra, E. Dobročka, A. Šatka, V. Buršiková, M. Držik, M. Zahoran, A. Plecenik, P. Kús, The influence of low-energy ion bombardment on the microstructure development and mechanical properties of TiB_x coatings, *Vacuum* 85 (2011) 866–870, <https://doi.org/10.1016/j.vacuum.2010.12.011>.
- [14] G. Greczynski, J. Lu, M.P. Johansson, J. Jensen, I. Petrov, J.E. Greene, L. Hultman, Role of Ti^{3+} and Al^{3+} ion irradiation ($n=1, 2$) during $Ti_{1-x}Al_xN$ alloy film growth in a hybrid HiPIMS/magnetron mode, *Surf. Coatings Technol.* 206 (2012) 4202–4211, <https://doi.org/10.1016/j.surfcoat.2012.04.024>.
- [15] V. Kouznetsov, K. Macák, J.M. Schneider, U. Helmersson, I. Petrov, A novel pulsed magnetron sputter technique utilizing very high target power densities, *Surf. Coatings Technol.* 122 (1999) 290–293, [https://doi.org/10.1016/S0257-8972\(99\)00292-3](https://doi.org/10.1016/S0257-8972(99)00292-3).

- [16] U. Helmersson, M. Lattemann, J. Bohlmark, A.P. Ehasarian, J.T. Gudmundsson, Ionized physical vapor deposition (IPVD): a review of technology and applications, *Thin Solid Films* 513 (2006) 1–24, <https://doi.org/10.1016/j.tsf.2006.03.033>.
- [17] K. Sarakinos, J. Alami, S. Konstantinidis, High power pulsed magnetron sputtering: a review on scientific and engineering state of the art, *Surf. Coatings Technol.* 204 (2010) 1661–1684, <https://doi.org/10.1016/j.surfcoat.2009.11.013>.
- [18] J.T. Gudmundsson, N. Brenning, D. Lundin, U. Helmersson, High power impulse magnetron sputtering discharge, *J. Vac. Sci. Technol. A Vacuum, Surfaces, Film.* 30 (2012), <https://doi.org/10.1116/1.3691832>.
- [19] A. Anders, Tutorial: Reactive high power impulse magnetron sputtering (R-HiPIMS), *J. Appl. Phys.* 121 (2017), <https://doi.org/10.1063/1.4978350>.
- [20] J.A. Hopwood, Plasma physics, in: 2000: pp. 181–207. doi: 10.1016/S1079-4050(00)80009-5.
- [21] J. Bohlmark, J. Alami, C. Christou, A.P. Ehasarian, U. Helmersson, Ionization of sputtered metals in high power pulsed magnetron sputtering, *J. Vac. Sci. Technol. A Vacuum, Surfaces, Film.* 23 (2005) 18–22, <https://doi.org/10.1116/1.1818135>.
- [22] B. Bakht, I. Petrov, J.E. Greene, L. Hultman, J. Rosén, G. Greczynski, Controlling the B/Ti ratio of TiB_x thin films grown by high-power impulse magnetron sputtering, *J. Vac. Sci. Technol. A Vacuum, Surfaces, Film.* 36 (2018) 030604, <https://doi.org/10.1116/1.5026445>.
- [23] G. Greczynski, I. Zhirkov, I. Petrov, J.E. Greene, J. Rosen, Gas rarefaction effects during high power pulsed magnetron sputtering of groups IVB and VIB transition metals in Ar, *J. Vac. Sci. Technol. A Vacuum, Surfaces, Film.* 35 (2017) 060601, <https://doi.org/10.1116/1.4989674>.
- [24] J. Palisaitis, M. Dahlqvist, L. Hultman, I. Petrov, J. Rosen, P.O.Å. Persson, On the nature of planar defects in transition metal diboride line compounds, *Materialia* 24 (2022) 101478, <https://doi.org/10.1016/j.mtl.2022.101478>.
- [25] J. Thörnberg, J. Palisaitis, N. Hellgren, F.F. Klimashin, N. Ghafoor, I. Zhirkov, C. Azina, J.-L. Battaglia, A. Kusiak, M.A. Sortica, J.E. Greene, L. Hultman, I. Petrov, P.O.Å. Persson, J. Rosen, Microstructure and materials properties of understoichiometric TiB_x thin films grown by HiPIMS, *Surf. Coatings Technol.* 404 (2020) 126537, <https://doi.org/10.1016/j.surfcoat.2020.126537>.
- [26] T. Wojcik, V. Ott, S. Özbilen, H. Leiste, S. Ulrich, P.H. Mayrhofer, H. Riedl, M. Stueber, Magnetron sputtered NiAl/TiB_x multilayer thin films, *J. Vac. Sci. Technol. A.* 40 (2022) 033410, <https://doi.org/10.1116/6.0001734>.
- [27] R. Psiuk, M. Milczarek, P. Jencyk, P. Denis, D.M. Jarząbek, P. Bazarnik, M. Pisarek, T. Mościcki, Improved mechanical properties of W-Zr-B coatings deposited by hybrid RF magnetron – PLD method, *Appl. Surf. Sci.* 570 (2021) 151239, <https://doi.org/10.1016/j.apsusc.2021.151239>.
- [28] M.A. Monclus, M.A. Baker, C. Rebholz, V. Stolojan, P.N. Gibson, A. Leyland, A. Matthews, Nanostructural studies of PVD TiAlB coatings, *Surf. Interface Anal.* 38 (2006) 731–735, <https://doi.org/10.1002/sia.2160>.
- [29] C. Rebholz, A. Leyland, J.M. Schneider, A.A. Voevodin, A. Matthews, Structure, hardness and mechanical properties of magnetron-sputtered titanium–aluminum boride films, *Surf. Coatings Technol.* 120–121 (1999) 412–417, [https://doi.org/10.1016/S0257-8972\(99\)00490-9](https://doi.org/10.1016/S0257-8972(99)00490-9).
- [30] J. Thörnberg, S. Mráz, J. Palisaitis, F.F. Klimashin, P. Ondracka, B. Bakht, P. Polcik, S. Kolozsvári, L. Hultman, I. Petrov, P.O.Å. Persson, J.M. Schneider, J. Rosen, Oxidation resistance and mechanical properties of sputter-deposited Ti_{0.9}Al_{0.1}B_{2.2} thin films, *Surf. Coatings Technol.* 442 (2022) 128187, <https://doi.org/10.1016/j.surfcoat.2022.128187>.
- [31] M. Stüber, H. Riedl, T. Wojcik, S. Ulrich, H. Leiste, P.H. Mayrhofer, Microstructure of Al-containing magnetron sputtered TiB_x thin films, *Thin Solid Films* 688 (2019) 137361, <https://doi.org/10.1016/j.tsf.2019.06.011>.
- [32] N. Nedfors, S. Mráz, J. Palisaitis, P.O.Å. Persson, H. Lind, S. Kolozsvári, J. M. Schneider, J. Rosen, Influence of the Al concentration in Ti–Al–B coatings on microstructure and mechanical properties using combinatorial sputtering from a segmented TiB₂/AlB₂ target, *Surf. Coatings Technol.* 364 (2019) 89–98, <https://doi.org/10.1016/j.surfcoat.2019.02.060>.
- [33] A. Mockute, J. Palisaitis, N. Nedfors, P. Berastegui, E. Broitman, B. Alling, L.-Å. Näslund, L. Hultman, J. Patscheider, U. Jansson, P.O.Å. Persson, J. Rosen, Synthesis and characterization of (Ti_{1-x}Al_x)B_{2+Δ} thin films from combinatorial magnetron sputtering, *Thin Solid Films* 669 (2019) 181–187, <https://doi.org/10.1016/j.tsf.2018.10.042>.
- [34] X. Cai, S. Ding, K. Wen, L. Xu, H. Xue, S. Xin, T. Shen, Unmasking the anomalous rapid oxidation of refractory TiB₂ at low temperatures, *J. Eur. Ceram. Soc.* 41 (2021) 5100–5108, <https://doi.org/10.1016/j.jeurceramsoc.2021.04.011>.
- [35] B. Bakht, J. Palisaitis, J. Thörnberg, J. Rosen, P.O.Å. Persson, L. Hultman, I. Petrov, J.E. Greene, G. Greczynski, Improving the high-temperature oxidation resistance of TiB₂ thin films by alloying with Al, *Acta Mater.* 196 (2020) 677–689, <https://doi.org/10.1016/j.actamat.2020.07.025>.
- [36] V. Šroba, T. Fiantok, M. Truchlý, T. Roch, B. Granić, K. Viskupová, L. Satrapinskyy, P. Švec, Š. Nagy, V. Izai, P. Kůš, M. Mikula, Structure evolution and mechanical properties of Al-alloyed tantalum diboride films prepared by magnetron sputtering co-deposition, *J. Vac. Sci. Technol. A.* 41 (2023) 023410, <https://doi.org/10.1116/6.0002390>.
- [37] T. Glechner, R. Hahn, A. Bahr, T. Wojcik, M. Weiss, J. Ramm, O. Hunold, P. Polcik, H. Riedl, Oxidation resistance of Si doped transition metal diborides at elevated temperatures, *Int. J. Refract. Met. Hard Mater.* 113 (2023) 106172, <https://doi.org/10.1016/j.jrhm.2023.106172>.
- [38] T. Glechner, H.G. Oemer, T. Wojcik, M. Weiss, A. Limbeck, J. Ramm, P. Polcik, H. Riedl, Influence of Si on the oxidation behavior of TM-Si-B_{2+x} coatings (TM = Ti, Cr, Hf, Ta, W), *Surf. Coatings Technol.* 434 (2022) 128178, <https://doi.org/10.1016/j.surfcoat.2022.128178>.
- [39] K. Macák, V. Kouznetsov, J. Schneider, U. Helmersson, I. Petrov, Ionized sputter deposition using an extremely high plasma density pulsed magnetron discharge, *J. Vac. Sci. Technol. A Vacuum, Surfaces, Film.* 18 (2000) 1533–1537, <https://doi.org/10.1116/1.582380>.
- [40] A.K. Agarwal, A. Garg, D.K. Srivastava, M.K. Shukla, Comparative wear performance of titanium based coatings for automotive applications using exhaust gas recirculation, *Surf. Coatings Technol.* 201 (2007) 6182–6188, <https://doi.org/10.1016/j.surfcoat.2006.08.145>.
- [41] J.C. Schuster, J. Bauer, The ternary system titanium-aluminum-nitrogen, *J. Solid State Chem.* 53 (1984) 260–265, [https://doi.org/10.1016/0022-4596\(84\)90100-2](https://doi.org/10.1016/0022-4596(84)90100-2).
- [42] J. Bohlmark, M. Lattemann, J.T. Gudmundsson, A.P. Ehasarian, Y. Aranda Gonzalvo, N. Brenning, U. Helmersson, The ion energy distributions and ion flux composition from a high power impulse magnetron sputtering discharge, *Thin Solid Films* 515 (2006) 1522–1526, <https://doi.org/10.1016/j.tsf.2006.04.051>.
- [43] B. Bakht, D. Primetzhof, E. Pitthan, M.A. Sortica, E. Ntemou, J. Rosen, L. Hultman, I. Petrov, G. Greczynski, Systematic compositional analysis of sputter-deposited boron-containing thin films, *J. Vac. Sci. Technol. A Vacuum, Surfaces, Film.* 39 (2021), <https://doi.org/10.1116/6.0001234>.
- [44] E. Lewin, J. Counsell, J. Patscheider, Spectral artefacts post sputter-etching and how to cope with them – A case study of XPS on nitride-based coatings using monoatomic and cluster ion beams, *Appl. Surf. Sci.* 442 (2018) 487–500, <https://doi.org/10.1016/j.apsusc.2018.02.191>.
- [45] G. Greczynski, L. Hultman, Towards reliable X-ray photoelectron spectroscopy: Sputter-damage effects in transition metal borides, carbides, nitrides, and oxides, *Appl. Surf. Sci.* 542 (2021) 148599, <https://doi.org/10.1016/j.apsusc.2020.148599>.
- [46] G. Greczynski, L. Hultman, X-ray photoelectron spectroscopy: Towards reliable binding energy referencing, *Prog. Mater. Sci.* 107 (2020) 100591, <https://doi.org/10.1016/j.pmatsci.2019.100591>.
- [47] C. Maszl, W. Breilmann, J. Benedikt, A. von Keudell, Origin of the energetic ions at the substrate generated during high power pulsed magnetron sputtering of titanium, *J. Phys. D. Appl. Phys.* 47 (2014) 224002, <https://doi.org/10.1088/0022-3727/47/22/224002>.
- [48] A. Anders, M. Panjan, R. Franz, J. Andersson, P. Ni, Drifting potential humps in ionization zones: the “propeller blades” of high power impulse magnetron sputtering, *Appl. Phys. Lett.* 103 (2013), <https://doi.org/10.1063/1.4823827>.
- [49] G. Greczynski, I. Petrov, J.E. Greene, L. Hultman, Paradigm shift in thin-film growth by magnetron sputtering: from gas-ion to metal-ion irradiation of the growing film, *J. Vac. Sci. Technol. A.* 37 (2019) 060801, <https://doi.org/10.1116/1.5121226>.
- [50] JCPDS International Centre for Diffraction Data, Aluminium Diboride (AlB₂) card 0 0-0 08-0216, (n.d.).
- [51] JCPDS International Centre for Diffraction Data, Titanium Diboride (TiB₂) card 00-035-0741, (n.d.).
- [52] A. Leyland, A. Matthews, On the significance of the H/E ratio in wear control: a nanocomposite coating approach to optimised tribological behaviour, *Wear* 246 (2000) 1–11, [https://doi.org/10.1016/S0043-1648\(00\)00488-9](https://doi.org/10.1016/S0043-1648(00)00488-9).
- [53] G. Greczynski, I. Zhirkov, I. Petrov, J.E. Greene, J. Rosen, Control of the metal/gas ion ratio incident at the substrate plane during high-power impulse magnetron sputtering of transition metals in Ar, *Thin Solid Films* 642 (2017) 36–40, <https://doi.org/10.1016/j.tsf.2017.09.027>.
- [54] G. Greczynski, I. Petrov, J.E. Greene, L. Hultman, Strategy for tuning the average charge state of metal ions incident at the growing film during HiPIMS deposition, *Vacuum* 116 (2015) 36–41, <https://doi.org/10.1016/j.vacuum.2015.02.027>.
- [55] B. Wicher, R. Chodun, G. Greczynski, A. Lachowski, M. Trzcinski, A.V. Pshyk, K. Król, K. Kulikowski, Ł. Skowroński, K. Zdunek, Carbon ion self-sputtering attained by sublimation of hot graphite target and controlled by pulse injection of a neon–helium gas mixture, *Appl. Surf. Sci.* 620 (2023) 156708, <https://doi.org/10.1016/j.apsusc.2023.156708>.
- [56] A. Anders, Tutorial: Reactive high power impulse magnetron sputtering (R-HiPIMS), *J. Appl. Phys.* 121 (2017) 171101, <https://doi.org/10.1063/1.4978350>.
- [57] S. Mertadam, M. Tanişli, N. Şahin, Investigation of branching fraction in the mechanically forced discharge region using optical emission spectrum, *Optik (stuttgart)* 260 (2022) 169065, <https://doi.org/10.1016/j.jjleo.2022.169065>.
- [58] J.T. Gudmundsson, Ionization mechanism in the high power impulse magnetron sputtering (HiPIMS) discharge, *J. Phys. Conf. Ser.* 100 (2008) 082013, <https://doi.org/10.1088/1742-6596/100/8/082013>.
- [59] J. Neidhardt, S. Mráz, J.M. Schneider, E. Strub, W. Böhne, B. Liedke, W. Möller, C. Mitterer, Experiment and simulation of the compositional evolution of Ti–B thin films deposited by sputtering of a compound target, *J. Appl. Phys.* 104 (2008), <https://doi.org/10.1063/1.2978211>.
- [60] Y.V. Martynenko, A.V. Rogov, V.I. Shul'ga, Angular distribution of atoms during the magnetron sputtering of polycrystalline targets, *Tech. Phys.* 57 (2012) 439–444, <https://doi.org/10.1134/S1063784212040196>.
- [61] G. Greczynski, L. Hultman, M. Odén, X-ray photoelectron spectroscopy studies of Ti_{1-x}Al_xN (0 ≤ x ≤ 0.83) high-temperature oxidation: The crucial role of Al concentration, *Surf. Coatings Technol.* 374 (2019) 923–934, <https://doi.org/10.1016/j.surfcoat.2019.06.081>.